Highlights

A chip-based 128-channel potentiostat for high-throughput studies of bioelectrochemical systems: optimal electrode potentials for anodic biofilms

Tom R. Molderez,Antonin Prévoteau,Frederik Ceyssens,Marian Verhelst,Korneel Rabaey

- A 128-channel potentiostat for high-throughput microbial electrochemistry
- Accompanying 128 gold electrode array (77 functional electrodes)
- Anodic electroactive biofilms simultaneously grown at 11 electrode potentials ($n = 7$)
- Midpoint potentials and charge transport parameters assessed by cyclic voltammetry
- Most performant EABs grown just below anodic plateau (-0.3 V and -0.25 V vs. Ag/AgCl)

A chip-based 128-channel potentiostat for high-throughput studies of bioelectrochemical systems: optimal electrode potentials for anodic biofilms

Tom R. Molderez[a,b,*], Antonin Prévoteau[b], Frederik Ceyssens[a], Marian Verhelst[a] and Korneel Rabaey[b]

[a]MICAS, KU Leuven, Kasteelpark Arenberg 10, 3001 Leuven, Belgium
[b]Center for Microbial Ecology and Technology (CMET), Ghent University, Coupure Links 653, 9000 Ghent, Belgium

ARTICLE INFO

Keywords:
Multichannel potentiostat
Electrode array
High-throughput experiment
Electroactive biofilm
Charge transport parameter

ABSTRACT

The presence of microorganisms performing extracellular electron transfer has been established in many environments. Research to determine their role is moving slowly due to the high cost of potentiostats and the variance of data with small number of replicates. Here, we present a 128-channel potentiostat, connected to a 128 gold electrode array. Whereas the system is able to perform simultaneously 128 (bio)electrochemical measurements with an independent electrical signal input, the present manufacturing of the array limited the number of effective channels for this study to 77. We assessed the impact of 11 electrode potentials ranging from −0.45 V to +0.2 V vs. Ag/AgCl (7 replicates per potential) on the growth and electrochemical characteristics of anodic electroactive biofilms (EABs) formed by acetate-fed microbial communities. After 7 days of growth, maximum current was reached for electrodes poised at −0.3 V, closely followed by −0.25 V and −0.1 V to +0.1 V, a range well-fitting the midpoint potential of minerals naturally reduced by electroactive bacteria such as *Geobacter Sulfurreducens*. There was no significant difference in apparent midpoint potential of the EABs (−0.35 V), suggesting that the mechanism of heterogeneous electron transfer was not affected by the electrode potential. The EABs poised below current plateau potential (≤ -0.3 V) exhibited slower growth but higher charge transfer parameters. The high-throughput and high reproducibility provided by the array may have a major facilitating impact on the field of electromicrobiology. Key aspects to improve are data processing algorithms to deal with the vast amount of generated data, and manufacturing of the electrode array itself.

1. Introduction

Electroactive microorganisms exchange electrons with minerals or solid electrodes and are found in many different environments (Potter, 1910; Logan et al., 2019). Some of these microorganisms can structure themselves in electroactive biofilms (EABs) and perform direct electron transfer (DET) with a conductive surface (Borole et al., 2011). Those EABs can be either anodic (transferring electrons from a metabolically oxidized substrate to an electrode) or cathodic (harvesting electrons from a cathode to perform a reduction). Several applications have been proposed for exploiting the unique ability of those microorganisms (Logan and Rabaey, 2012; Beyene et al., 2018; Wang et al., 2020). In a microbial fuel cell, microorganisms oxidize biodegradable organic compounds and transfer the corresponding low potential electrons to an anode, allowing for small electric power generation while treating wastewater (Logan et al., 2006). Microbial electrosynthesis uses external power to drive microbial metabolism into producing valuable organic components in a cathodic compartment of an electrolysis cell (Rabaey and Rozendal, 2010). Microbial electrodes have been proposed as a novel amperometric biosensor for bioprocess or environmental monitoring due to the fast response of their current towards environmental changes (Prévoteau and Rabaey, 2017). Almost all processes still suffer from low performance, and mechanisms behind DET are not fully unresolved (Shi et al., 2016). This has stimulated both

*Corresponding author
tom.molderez@esat.kuleuven.be (T.R. Molderez); Antonin.Prevoteau@UGent.be (A. Prévoteau); Frederik.Ceyssens@esat.kuleuven.be (F. Ceyssens); Marian.Verhelst@esat.kuleuven.be (M. Verhelst); Korneel.Rabaey@UGent.be (K. Rabaey)
www.esat.kuleuven.be/micas/ (M. Verhelst); www.cmet.ugent.be/ (K. Rabaey)
ORCID(s): 0000-0002-4171-2755 (T.R. Molderez); 0000-0001-8430-4412 (A. Prévoteau); 0000-0002-9381-3398 (F. Ceyssens); 0000-0003-3495-9263 (M. Verhelst); 0000-0001-8738-7778 (K. Rabaey)

Table 1
Overview of recent studies of the impact of the electrode potential on biofilm growth and characterization. References are (1) (Finkelstein et al., 2006), (2) (Parot et al., 2008), (3) (Busalmen et al., 2008), (4) (Torres et al., 2009), (5) (Wei et al., 2010), (6) (Carmona-Martínez et al., 2013), (7) (Zhu et al., 2013), (8) (Bosch et al., 2014), (9) (Ishii et al., 2014), (10) (Dennis et al., 2016), (11) (Kato, 2017), (12) (Pinto et al., 2018).

Reference	Inoculum	set potentials [V] vs. Ag/AgCl (number of potentials)	Replicates	max j_{cat} [$\mu A\,cm^{-2}$]	Correlation E vs. j_{cat} (E for max j_{cat})
(1)	Mixed	−0.06, +0.1 and +0.62 (3)	3	450	Positive (+0.62)
(2)	Mixed	+0.33, +0.53 and +0.73 (3)	1	15	Negative (+0.33)
(3)	*G. Sulfurreducens*	+0.1 and +0.6 (2)	na	10	Positive (+0.6)
(4)	*G. Sulfurreducens*	−0.36, −0.3, −0.19 and +0.17 (4)	2	0.8	Negative (−0.36)
(5)	*G. Sulfurreducens*	−0.37, −0.21 and +0.2 (3)	5	207	Positive (+0.2)
(6)	*S. Putrefaciens*	$-0.1, 0, \ldots, +0.4$ (6)	3	12	Positive (+0.4)
(7)	Mixed	−0.25, −0.09, +0.21, +0.51 and +0.81 (5)	2	na	Optimum (+0.21)
(8)	*G. Sulfurreducens*	$-0.31, -0.17, \ldots, +0.4$ (6)	3	400	Optimum (−0.03)
(9)	Mixed	−0.41, −0.31 and +0.29 (3)	1	358 ± 3	Positive (+0.29)
(10)	Mixed	+0.09, +0.34 and +0.59 (3)	1	175	Optimum (+0.34)
(11)	*G. Sulfurreducens*	$-0.5, -0.4, \ldots, +0.2$ (8)	3	236 ± 25	Optimum (−0.2)
(12)	*S. Oneidensis*	−0.3, +0.3, +0.5 (3)	1	120	Positive (+0.5)
This work	Mixed	$-0.45, -0.4, \ldots, -0.1, 0, \ldots, +0.2$ (11)	7	769 ± 41	Optimum (−0.3)

fundamental level and applied research (Kracke et al., 2015; Levar et al., 2017; Kumar et al., 2017). Unfortunately, research progression is slow because of the challenges with the dedicated experimental setups. Experiments with EABs typically last from days to months (Prévoteau et al., 2019), often with high variability between replicates, especially when EABs are grown in separate reactors. Furthermore, the potentiostats needed to control the electric input and characterize the electrochemical properties of EABs are expensive, with a premium price-per-channel in the order of 1000–10 000 US$. While several commercial potentiostat medium-throughput systems (up to 32 dedicated channels in a single device) have been presented, potentiostat prices-per-channel have not dropped considerably. This makes it yet unfeasible to perform high-throughput EAB studies. This high-throughput approach, as shown in other research fields, such as cellular impedance, has major benefits (Ferrer et al., 2017; Mira et al., 2019). Thus, the combination of long experiment time and expensive equipment severely limits experiment throughput.

For example, current studies are generally capable of simultaneously testing only 3 to 8 individual electrochemical potentials with only up to 3 replicates in the best case. A brief overview of the most recent studies of the correlation between the potential and the current is given in Table 1. A more detailed overview can be found in (Wagner et al., 2010). Those low-throughput methods often induce a substantial variation in results and associated conclusions which impedes true progress in the field of microbial electrochemistry. For example, multiple studies have reported the impact of constant electrode potential on the development and performance of anodic EABs without scientific consensus even for identical pure cultures or comparable mixed-communities. Furthermore, while all the aforementioned studies reported an impact of constant electrode potentials, it has been shown that growing anodic EABs under periodic polarization of the underlying electrode could substantially improve the conductivity and overall performance of the EABs (Zhang et al., 2018, 2019). The fact that a dynamic electrical input could also be used to optimize EABs tremendously increases the number of relevant test available, as now also the frequency of polarity switching becomes a key parameter.

All the aforementioned reasons call for high-throughput systems allowing for simultaneous testing of multiple electric signals with a sufficient number of technical replicates. This work proposes the use of advanced microelectronics, driven by the well-known Moore's law (Moore, 1965), for designing an affordable potentiostat able to simultaneously perform up to 128 static or dynamic electrochemical experiments to grow and characterize EABs. Recently, several low-cost ($<$ 100 US$-per-channel) potentiostats have been proposed although all only contain at most 8 individual channels (Vergani et al., 2012; Ramfos et al., 2013; Zhao et al., 2013; Hu et al., 2016; Stradolini et al., 2016; Linhardt et al., 2018; Pruna et al., 2018; Molderez et al., 2019). Because of the tremendous speed difference between modern electronics and the studied microorganism responses, a time-division multiplexed potentiostat channel architecture allowed for an instrument with 16 times more channels at a 4 times lower cost per channel than the state of the art (Molderez et al., 2020). The accompanying 128 gold electrode array was designed using lithography technology on

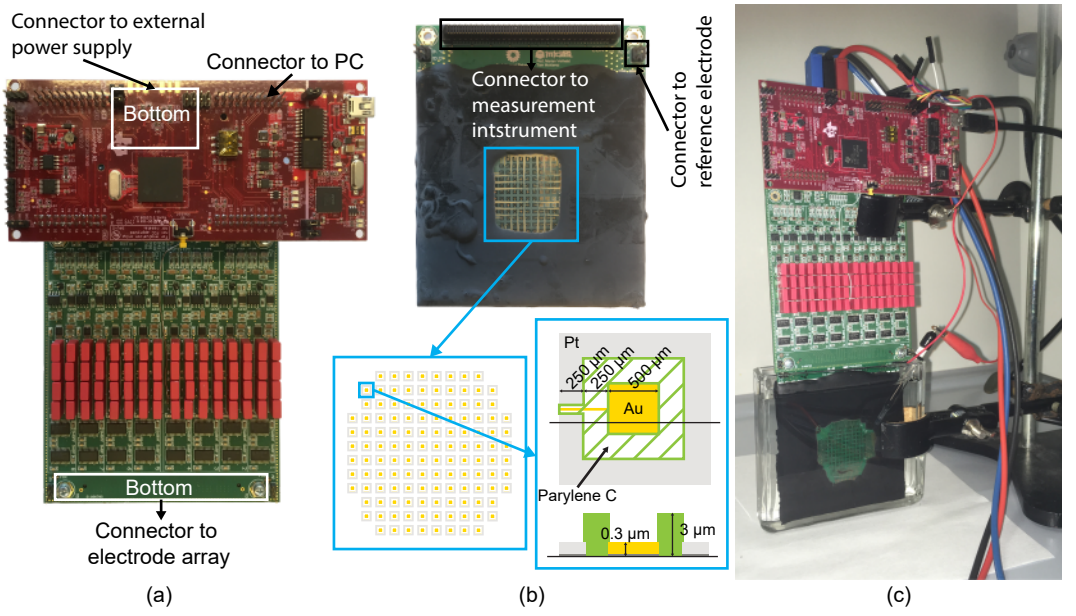

Figure 1: High-throughput electrochemical system with (a) top view of the 128-channel potentiostat with a connector to the PC for data monitoring and a connector to the 128-electrode array, (b) top view and scheme of the 128-electrode array consisting of 128 gold working electrodes (0.5×0.5 mm^2) surrounded by a common platinum counter electrode, and (c) a full electrochemical setup with the 128-electrode array immerged in an electrolyte with a single reference electrode.

a separate board with flexible interconnection to the measurement instrument. Here we used this high-throughput system to assess the impact of the electrode potential on the growth and electrochemical performance of acetate-fed anodic mixed-community EABs. Due to current manufacturing challenges, only 77 electrodes showed identical behavior during an abiotic verification experiment and were therefore used to grow EABs at 11 constant potentials ranging from -0.45 V to $+0.2$ V vs. Ag/AgCl, with 7 replicates per potential. Cyclic voltammetry scans were recorded under both turnover (acetate saturation for EAB) and nonturnover (acetate-depleted) conditions to assess the apparent midpoint potential and the charge transport parameter of the respective EABs. The impact of the electrode potential on the final EAB volume was finally assessed by confocal microscopy. The vast amount of data recorded with sufficient replicates during a single experiment strengthen statistical significance and opens new opportunities for the field of electromicrobiology.

2. Materials and methods

2.1. Experiment setup

The experiment setup, shown in Fig. 1, consists of three units: the 128-channel potentiostat, the 128-electrode array and the bioreactor.

2.1.1. The 128-channel potentiostat

A custom-designed, 128-channel potentiostat was used for EAB growth and electrochemical analysis (Fig. 1a). A detailed discussion of the hardware architecture is given in our previous work (Molderez et al., 2020). A Delfino microprocessor (F28379D, Texas Instruments) was used to simultaneously and independently control the potential of the working electrodes (WEs) of the array, and to transfer the data to the PC. The data was visualized in real-time using MATLAB® for debugging purposes. Control of the instrument settings and experiment execution was done using a command line interface in MATLAB®. The large number of channels made the use of a GUI impractical. The DC current and voltage circuitry of each channel was calibrated before use with a source meter (2450 SourceMeter, Keithley) resulting in a relative error below 1 % for both current and voltage. The platform component cost was only 600 US$ resulting in a cost-per-channel of 5 US$.

2.1.2. The 128-electrode array

The 128-electrode array for EAB growth was external to the measurement board to allow testing of different electrode arrays (Fig. 1b). The used 128-electrode array contained 128 WEs and 128 counter electrodes (CEs). The CEs are all connected to the electronic ground potential. Each square WE measured 0.5×0.5 mm^2 and used gold as top layer material. A box-shaped platinum CE surrounded each WE, with a 250 µm insulated gap between WE and CE and 250 µm width with a small opening for routing (Fig. 1b). The WE interelectrode distance, i.e. the center-to-center distance, (both horizontal and vertical) was 2.5 mm. The used technology for the 128-electrode array production was lithography. A 3 inch diameter glass Pyrex 7740 wafer was thoroughly rinsed with acetone, isopropanol and deionized water, successively, then ultrasonicated for 15 min in deionized water and dried with N_2 gas. Lift-off was used for deposition of the platinum layer. The wafer was dehydrated for 5 min at 200 °C on a hotplate. Next, HDMS (3000 rpm, 45 s), lor10B (3000 rpm, 45 s then soft baked at 180 °C for 5 min) and S1818 (4000 rpm, 45 s, then soft baked at 110 °C for 1 min) were successively spun and baked on a hotplate. The wafer was exposed with 42 mJ m^{-2} (wavelength 365 nm) using a chrome-on-glass-mask. Development was done in 351 developer, diluted 1:3 by volume in water. Then, a thin titanium adhesion layer was deposited (60 s, 200 W) and next a platinum layer (5 min, 80 W) using RF magnetron sputtering (Balzers BAE370). Lift-off was done in NMP overnight. Gold was deposited using the same procedure. Only the sputter parameters of the gold were different (3 min, 100 W). Next, the wafer was completely coated with 3 µm of Parylene C (Plasma Parylene Systems Labcoater 300). The electrodes were etched free using the following protocol. The wafer was soft-baked for 5 min at 200 °C. Next, HDMS (3000 rpm, 45 s) and ma-P1275 (3000 rpm, 30 s, then soft-baked at 120 °C for 2 min) were spun. Exposure was done using 300 mJ m^{-2} (365 nm wavelength) using a second chrome-on-glass mask to define the electrode openings in the Parylene C. Reactive-ion etching was done for 35 min at 100 W. The sample was diced and aluminum wire bonded to a separate printed circuit board (PCB), with an interface to the 128-channel PCB. The full PCB was coated with epoxy (EO1016 QTX, Loctite) for electrical isolation and protection of the bondwires. An abiotic electrochemical control was performed with a dissolved redox probe (ferrocyanide) to verify the correct operation and the reproducibility of the electrodes response (section S2).

2.1.3. Reactor setup

The bioelectrochemical experiments were performed in a single-chamber, batch-fed, cylindrical 700 mL glass reactor. The reactor was placed in an anaerobic workstation (GP-Campus, Jacomex, TCPS NV, Rotselaar, Belgium) under a N_2:CO_2 (90:10, v/v) atmosphere controlled at 28 °C. The reactor was filled with 500 mL of modified M9 medium (pH 7.5) including 24 mM sodium acetate as electron donor for the EABs (Guo et al., 2013). An Ag/AgCl reference electrode was immerged in the electrolyte in close proximity of the 128-electrode array (ALS, Japan, 3 M KCl, +0.205 V vs. standard hydrogen electrode at 28 °C). The electrolyte was continuously mixed with a magnetic stirrer rotating at 100 rpm. The reactor was inoculated with 25 mL (5 vol%) of fresh anolyte effluent from a continuous, acetate-fed bioelectrochemical system (Guo et al., 2017) and the electrodes were immediately polarized at their respective potential.

2.2. Bioelectrochemical experiments

The total experiment lasted 300 h (Fig. 2a) with first an initial EAB growth monitored by chronoamperometry until most current started to stabilize (142 h). Next, turnover (t = 142 h) and nonturnover (t = 164 h) CVs were recorded for all electrodes. A second cycle of growth was carried out until the current dropped to almost zero (300 h). A second nonturnover CV was then recorded (324 h). Finally, the biofilm volume was derived from confocal microscopy imaging. Electrode potentials are, unless explicitly stated, referred to the Ag/AgCl reference electrode used in this work.

2.2.1. Initial EAB growth

The bioelectrochemical experiment was simultaneously performed with 77 electrodes to assess the impact of 11 constant electrode potentials (7 replicates per potential). The electrodes were during 142 h poised at: −0.45 V, −0.4 V, −0.35 V, −0.3 V, −0.25 V, −0.2 V, −0.15 V, −0.1 V, 0 V, +0.1 V and +0.2 V vs. Ag/AgCl. The current output was internally sampled by chronoamperometry at 651 Hz and before being transmitted to an external PC, downsampled 2048 times by averaging. During post-processing, outliers were removed using a moving median filter (window size of 2 h), Gaussian lowpass filtered (window size of 2 h) and subsampled to one sample per hour.

For each of the 11 potential groups, the average current density was reported. Outliers, i.e. electrodes that showed no growth, were removed from the dataset and reported separately. For one anode potential setting, −0.4 V, only a

single electrode showed EAB growth and thus no standard deviations could be calculated. The averaged current density was either integrated over time for each group to obtain the average of total accumulated charge, or differentiated for each group to obtain the increase rate in current. The maximum current densities for the first growth cycle were calculated from the averaged current between $t = 141$ h and $t = 142$ h.

2.2.2. Intermediate turnover and nonturnover CVs recording

Turnover CVs were run 142 h after inoculation and polarization, once most catalytic currents had started to stabilize. They were carried out with a scan-rate of 5 mV s^{-1}, 10 mV s^{-1} and 20 mV s^{-1}, from −0.65 V to +0.3 V and with at least three successive cycles. The current output was internally sampled at 651 Hz and downsampled 32 times by averaging. During post-processing, the current output was further subsampled to one sample per 10 mV. Represented CVs and corresponding data are from the third cycle. Anodic plateau currents were calculated from the averaged current between +0.2 V and +0.25 V of the CV recorded at 5 mV s^{-1}. The apparent midpoint potential $E_{1/2}$ was derived from the average of the inflection point of the forward and backward scan CV, i.e. the half wave potential of the sigmoid polarization curves (Fig. S6) (Espinoza et al., 2019).

After these turnover CVs, the electrodes were placed in a second, equal setup but with acetate-free M9 to perform nonturnover CVs. The current was allowed to stabilize close to zero for 22 h before performing the nonturnover measurements to extract a charge transport parameters across the EABs ($t = 164$ h after inoculation) (Zhang et al., 2017). The scan rates were 10 mV s^{-1}, 20 mV s^{-1}, 40 mV s^{-1}, 60 mV s^{-1}, 80 mV s^{-1}, 100 mV s^{-1}, 120 mV s^{-1}, 140 mV s^{-1}, 160 mV s^{-1}, 180 mV s^{-1} and 200 mV s^{-1} from −0.65 V to +0.3 V. The current output was internally sampled at 651 Hz and downsampled 32 times by averaging. During post-processing, the current output was further subsampled to one sample per 10 mV. Represented CVs and corresponding data are from the third cycle. The charge transport parameter $CD_{app}^{1/2}$ (i.e. the product of an apparent charge carrier concentration C by the square root of the apparent diffusion coefficient for the electrons D_{app}) was derived from the Randles-Ševčík equation (Katuri et al., 2012; Bonanni et al., 2013; Jana et al., 2014; Zhang et al., 2017). For all scan rates, the maximum current and background current of the forward scan were extracted and averaged over multiple cycles to obtain the anodic peak currents. The charge transport parameter was estimated from the linear regression between those peak currents and the square root of the scan rate at which they were recorded (Fig. S10).

2.2.3. Second cycle of growth with acetate and associated measurements

After the turnover and nonturnover CV experiments, the electrodes were placed in a third, equal reactor, with 24 mM acetate for a second growth period (144 h to 300 h), with identical experiment conditions and settings. During this second cycle, the maximum current density (averaged over one hour) of each electrode potential was recorded. When current started dropping (after 300 h since inoculation), the electrodes were for a fourth time transferred to an equal reactor (without acetate) for a second set of nonturnover CVs after 324 h (with equal settings as the first set).

2.2.4. Confocal fluorescence microscopy experiments

Live-dead staining was done on hydrated EABs at the end of the experiment using a previously described protocol (Zhang et al., 2017). The EABs were visualized with a Nikon A1R confocal laser scanning microscopy (ten times magnified with an air lens with numerical aperture of 0.45). A complete Z-stack was made of at least 3 electrodes for each of the 11 distinct potentials, although for some electrodes (indicated in Fig. S12), the staining procedure failed, resulting in no reported standard deviations. The surface electrode plane coincided with the focal planes of the confocal microscope. Illumination thus occurred perpendicular on the electrode plane. The 3D biofilm volume was estimated using MATLAB®. The image was 3D Gaussian filtered to remove noise. Locations with a clear staining error were manually removed. The image was then coarsely divided into a biofilm region and a non-biofilm region. A plane was fit through the non-biofilm region, i.e. the bottom of the electrode, to compensate for tilting. The biofilm border was defined as the region of maximum intensity. Knowing the electrode surface and the biofilm border, the height of each pixel of the biofilm was calculated from the difference between the biofilm border and the electrode surface, multiplied by the z-step and a correction factor for the (air-liquid) refraction (Bakke and Olsson, 1986; Dirckx et al., 2005; Besseling et al., 2015). Finally, the volume was calculated by summing all heights and multiplying them with the area of each pixel.

3. Results and discussion

3.1. Initial growth of EABs

The relevant potentials to be explored were determined based on existing studies (Table 1) and the observed CV of the EABs (Fig. S7), resulting in a potential between −0.45 V to +0.2 V (Levar et al., 2017). This spans the full potential range of a typical sigmoid polarization curve for acetate-fed microbial anodes, including several potentials within the anodic plateau which is reached at −0.22 V. From the electrochemical verification experiment of the 128-electrode array, only 77 operated correctly with reproducible results (see section S1), which associates with the non-optimized manufacturing procedure, the manual production approach and the low number of manufactured samples. Further optimizing the manufacturing parameters in a more automated production environment with larger sample sizes would ameliorate the number of correctly operating electrodes. Nevertheless, this number allowed to explore 11 different potentials to grow EABs with 7 replicates per potential.

About 25 h after inoculation, the catalytic current density started increasing exponentially on most electrodes (60 out of 77), illustrating the colonization of their surface by electroactive bacteria and the growth of EABs (Fig. 2b shows the average current density, Fig. S2 shows the individual chronoamperometries). Exponential growth lasted until $t \approx 70$ h. From then, the catalytic currents increased almost linearly until $t = 140$ h, at which they started to stabilize for most electrodes. For any set of electrodes poised at a specific potential, the maximal standard deviation of the catalytic current density remained below 50 µA cm^{-2} i.e. a relative standard deviation ≤ 10 % (except for the extreme anode potentials of −0.45 V, −0.4 V and +0.2 V) (Fig. S3). Current production was minimal at extreme electrode potentials (−0.45 V and +0.2 V) and lower on electrodes −0.4 V and −0.35 V (Fig. 2c) which explains the higher relative variability. The 5 sets of electrodes poised at potentials ranging from −0.2 V to +0.1 V exhibit very similar current evolution and maximum current reached [$\approx (540 \pm 23)$ µA cm^{-2}]. This is not surprising considering that all potentials are positioned on the anodic plateau of the sigmoid polarization curve (assuming that the polarization curves stay invariable with the growth potential—*vide infra*). As such, from a kinetic perspective, the flux of electrons entering the electron transport chain of the electroactive microorganism(s) is maximized at those potentials. Furthermore, following a classic Nernstian model, one can assume that the redox protein(s) performing the heterogeneous electron transfer are fully oxidized at the electrode interface polarized within the plateau potential (Zhang et al., 2017). From a thermodynamics point of view, this maximizes the oxidized ratio of the intracellular redox partners involved in electron transport, and ultimately of the NAD^+/NADH couple directly involved in energy generation, allowing for the electroactive bacteria to fully exploit the thermodynamic frame coupling acetate oxidation and DET (Korth and Harnisch, 2019). By maximizing both the electron transfer rate and presumably the amount of energy per electron, it appears reasonable that EAB grown at plateau potentials exhibit very similar and highest initial growth rate and associated current development. Conversely, a very different behavior was observed for EAB grown at the highest potential tested of +0.2 V vs. Ag/AgCl. Here the current evolution was much slower, and the maximum current reached after 140 h was only (32 ± 6) µA cm^{-2}, which is 6 % of the current produced by the EABs grown at all lower plateau potentials. Here a more complex phenomenon than simple kinetics and thermodynamics considerations must likely be at stake and a similar observation of lower performance at high electrode potentials (in this case of +0.6 V vs. Ag/AgCl) was made earlier (Dennis et al., 2016). One may note that +0.2 V was the only potential tested that is *above* the −0.37 V to 0.15 V vs. Ag/AgCl range for apparent midpoint potentials of solid Fe and Mn (hydr-)oxides reducible by *G. Sulfurreducens* (Levar et al., 2017), the model organism for anodic DET. Though we did not assess the microbial community in the present study, our acetate-fed EABs were always having *Geobacter* spp. as most abundant taxon at the genus level (Guo et al., 2013; Zhang et al., 2017, 2018, 2019), which include species that are mostly known for their metal reduction capabilities. One may speculate that the redox partners (presumably c-type cytochromes) performing the DET may not be evolutionary optimized to give electrons at such high potentials, and that electroactive bacteria may detect/adhere/grow better on electrodes poised at potentials similar to those of their natural solid terminal electron acceptors. Further investigation including electrodes poised at even higher potentials would help unravel this phenomenon.

The current produced by EABs grown just below the anodic plateau potential, at −0.25 V, evolved similarly than those poised at plateau potentials, but reached a slightly higher maximal current at $t = 140$ h [$\approx (650 \pm 23)$ µA cm^{-2} vs. $\approx (540 \pm 23)$ µA cm^{-2}]. At the lower potential −0.3 V, the current evolution was substantially delayed, but then increased faster than for any other EAB after $t \approx 70$ h (Fig. 3a) for reaching (625 ± 47) µA cm^{-2} after 140 h of polarization. The delay in initial current evolution was further increased when lowering the electrode potential (−0.35 V and −0.4 V). This longer lag phase appears rational considering these conditions of restricted energy harvest for the

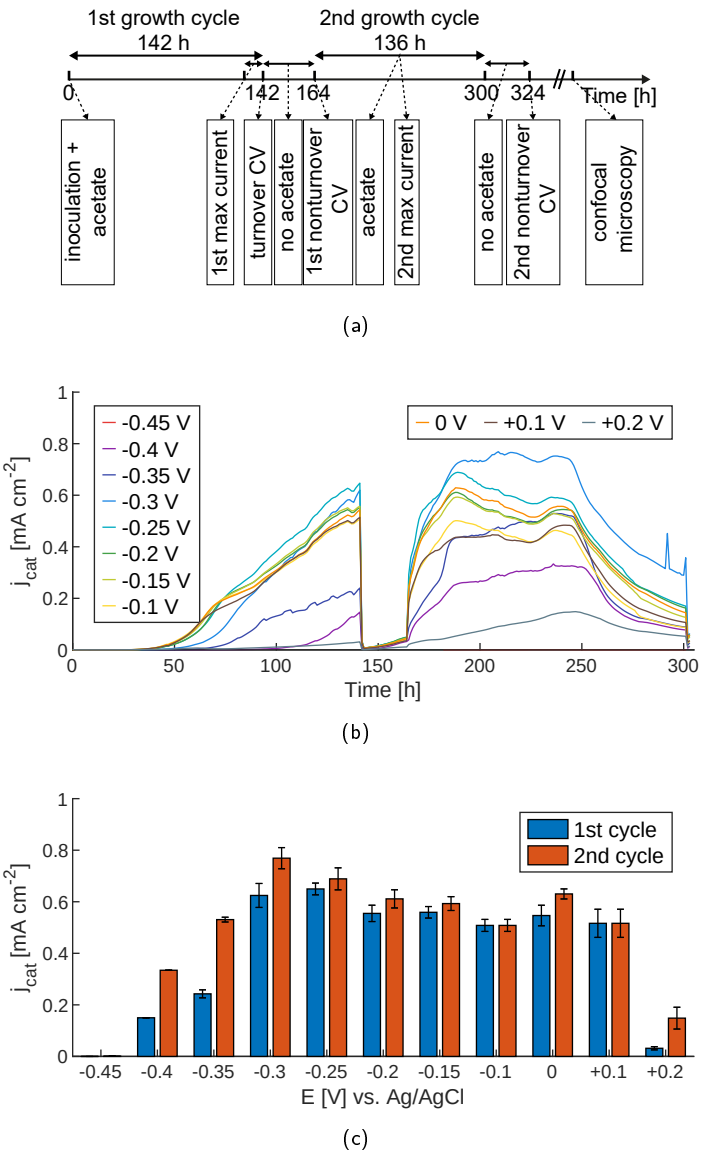

Figure 2: (a) Experiment timeline for the 77 electrodes with the first and second growth cycle. (b) Evolution of the catalytic current density over time for the different electrode potentials (n = 7). The average for each potential is represented; $t = 0$ corresponds to the inoculation. (c) Maximum catalytic current density reached during the first and second growth cycle (n = 7).

electroactive bacteria (Korth and Harnisch, 2019).

3.2. First turnover and nonturnover CV experiments

A set of turnover CVs were carried out at $t = 142$ h to assess the current-potential relation (Fig. 3c and Fig. S5). The turnover CVs exhibited the usual sigmoid curves observed for *Geobacter spp.* (dominated or pure) EABs for all active electrodes, except for the single EAB grown at the lowest potentials of −0.45 V and −0.4 V where transient features (peaks) overcome the small "steady-state" catalytic feature (sigmoid). The well-defined sigmoid shapes illustrate the occurrence of a kinetically non-limiting (quasi-)reversible heterogeneous electron transfer at the EAB/electrode interface (Snider et al., 2012; Zhang et al., 2017). The anodic plateaus of all polarization curves were reached at about −0.22 V vs. Ag/AgCl. The only significant difference in the shape of the turnover CVs of identical scan rate appears to be the extent of small transient peaks at the beginning of the anodic plateau (Fig. 3c and Fig. S5). Those were

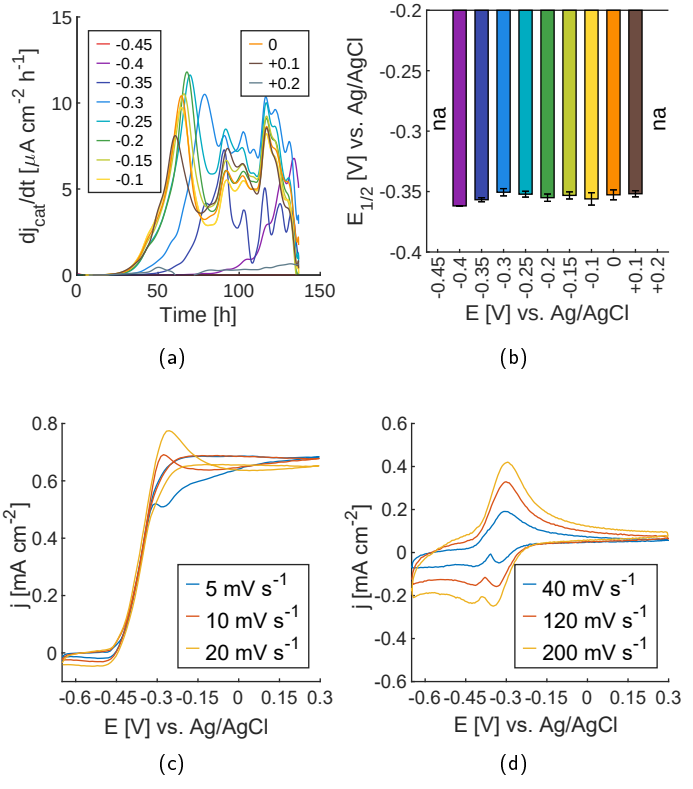

Figure 3: (a) Average catalytic current rate of the EABs in the first cycle for each of the 11 different anode potentials ([V] vs. Ag/AgCl) (n = 7), (b) apparent midpoint potential (average and standard deviation) of the EABs in the first cycle (n = 7), (c) representative turnover cyclic voltammetry scan (electrode 1 of −0.3 V), and (d) representative nonturnover cyclic voltammetry scan of the same electrode.

substantially larger for EABs grown at lower potentials (≤ -0.3 V) i.e. at potentials below the anodic plateau. This could be due to a larger amount (or concentration) of redox partners for the EABs grown at those lower potentials, implying a larger charge storage ability and therefore larger relative contribution of the transient peaks with respect to the "steady-state" catalytic current represented by the sigmoid. A somehow unexpected feature of the turnover CV of the EABs grown at lowest potential (−0.4 V and −0.35 V), for which we do not have an explanation, was that their anodic plateau current was lower than the catalytic current just previously recorded during the chronoamperometry at their respective potential, conversely to what would be expected from a conventional Nernstian electrochemical system (Fig. S8).

Figure 3b shows the extracted global midpoint potential ($E_{1/2}$) for the turnover CVs. Recordings for −0.45 V were unreliable due to the non-sigmoid shape of the corresponding turnover CV. The value for $E_{1/2}$ was −0.35 V for all other potentials of growth, which corresponds well with the existing literature for either *Geobacter sulfurreducens* or *Geobacter spp.* dominated EABs (Richter et al., 2009; Virdis et al., 2014; Dennis et al., 2016; Zhang et al., 2017). The identity of $E_{1/2}$ for all EABs suggests that the applied electrode potential did not impact the nature of the main redox partner(s) performing the heterogeneous electron transfer.

The 128-electrode array was then transferred to an acetate free medium to successively record nonturnover CVs at different scan rates (Fig. 3d and Fig. S9). Usual redox peaks were displayed surrounding the apparent midpoint potential of −0.35 V. The amplitude of the redox peaks is associated with the amount (and/or concentration) of the microbially produced charge carriers and the ability of the EABs to transport electrons across their conductive matrix. The anodic peak currents were increasing linearly with the square root of the scan rate (Fig. S10), as predicted by the classic model of charge transport involving a semi infinite diffusion process (Snider et al., 2012; Yates et al., 2015; Zhang et al., 2017, 2019). From the Randles-Ševčík equation, one can derive a charge transport parameter

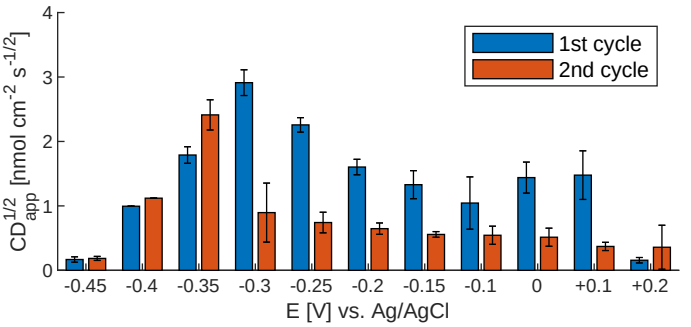

Figure 4: Charge transport parameter (average and standard deviation) of the EAB after the first cycle (blue) and after the second cycle (red) (n = 7).

characteristic of the conductivity of the EABs ($C \times D_{app}^{1/2}$), where C would correspond to an average concentration of charge carriers (in electron equivalent) and D_{app} an apparent diffusion coefficient for the electrons (Zhang et al., 2017) across the EAB. Electrodes that were poised at both extreme potentials (−0.45 V and +0.2 V) did not exhibit clear redox peaks, and no estimations are therefore provided. Only one electrode at −0.4 V showed peaks, resulting in the absence of a standard deviation. The charge transport parameter was similar for EABs grown at plateau potentials (from −0.2 V to +0.1 V) at (1.4 ± 0.3) nmol cm^{-2} s$^{-1/2}$. It was higher for EABs grown slightly below the plateau potential (from −0.35 V to −0.25 V), with a maximum of (2.9 ± 0.3) nmol cm^{-2} s$^{-1/2}$ for EABs grown at −0.3 V. This suggests that those EABs grown at "suboptimal potentials" may be more concentrated in charge carriers and/or more conductive than their counterparts grown at plateau potentials. Poising electrodes at those suboptimal potentials induces a relative limitation in electron acceptor availability for the electroactive microorganisms. Planktonic *Geobacter sulfurreducens* has been shown to overexpress c-type cytochromes (charge carriers presumably involved in electron transport mechanism) when under electron acceptor limitation (Bansal et al., 2013). We also observed that charge carriers concentrations increased by more than 3 times in acetate-fed EABs periodically polarized at plateau potential and left under open circuit (i.e. periodically under electron acceptor limitation) (Zhang et al., 2018). Similarly, an increase in catalytic current was observed for O_2-reducing microbial cathodes poised at a "suboptimal potential" close to the $E_{1/2}$ of their sigmoid polarization curve (Leary et al., 2015). All those results suggest that electroactive bacteria may compensate for the lower electron flux (and presumably the lower energy per electron) induced by suboptmal potentials, by overexpressing redox partners involved in the mechanisms of extracellular electron transfer. This could be attractive to increase resolution of such measurements in a context of e.g. sensor systems. Finally, the Bond group has shown that to optimize energy harvest, *Geobacter sulfurreducens* can express different inner membrane cytochromes to extract electrons from their quinone pool depending on the redox potential of its solid final electron acceptor (Levar et al., 2014; Zacharoff et al., 2016; Levar et al., 2017). The critical electrode potential at which one or another electron pathway is favored, was found to be −0.1 V vs. SHE (i.e. −0.305 V vs. Ag/AgCl). They suggest that this ability to use different inner redox pathways depending on electrode potential may represent a common trait amongst *Geobacter* strains (Joshi et al., 2019). We cannot exclude that a similar selection of optimal electron transport chain occurred for our electroactive microorganisms, ultimately leading to different maximum current densities.

3.3. Second growth cycle and second nonturnover CV experiments

The electrodes were transferred to a third equal reactor with 24 mM sodium acetate for a second growth cycle and were poised at their previous respective potential. The catalytic current density of all electrodes that previously showed electroactivity mostly recovered after about 10 h of polarization (Fig. 2b), while other electrodes did not start to produce catalytic current. Between $t = 180$ h and $t = 250$ h, all active electrodes reached a maximum, relatively stable current density plotted on Figure 2c. Similarly than for the first growth cycles, the electrodes poised at plateau potential (≥ -0.2 V vs. Ag/AgCl) reached almost identical maximum currents of (572 ± 56) µA cm^{-2} (n = 35 electrodes) except for the highest potential of +0.2 V for which the current density was much lower at (149 ± 42) µA cm^{-2}. The maximum current was very similar between the first and second cycle for electrodes poised between −0.2 V to +0.1 V. Conversely, it substantially increased during the second cycle for the 21 EABs polarized below plateau potential (−0.4 V to −0.3 V). The relative enhancement of the current between the two cycles increased when the potential decreased, confirming

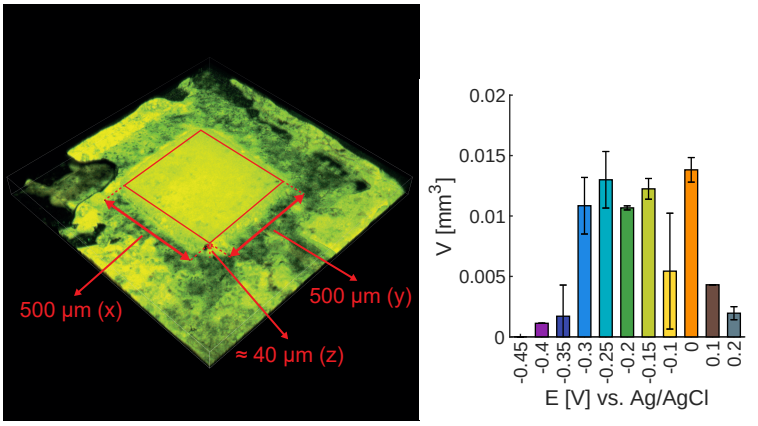

Figure 5: (a) Fluorescence 3D image of a representative EAB (Electrode 1 of −0.3 V vs. Ag/AgCl). (b) Volume of hydrated EABs at the end of the experiment (n = 3).

the hypothesis of lower growth and/or electroactivity improvement at those lower potentials. The two highest catalytic current densities were reached for electrodes poised at −0.3 V [(769 ± 41) µA cm^{-2}] and −0.25 V [(650 ± 23) µA cm^{-2}, n = 7], i.e. the two first potentials studied below the plateau of the polarization curves. These electrodes also generated the largest total charge (Fig. S4). After t = 250 h, the current density of all electrodes decreased probably because of acetate depletion. At 300 h, the electrodes were transferred to a fourth equal reactor without acetate to perform a second set of nonturnover CVs (Fig. S11). The charge transport parameter ($C \times D_{app}^{1/2}$) substantially decreased between the two growth cycles for the EABs polarized between −0.3 V to +0.1 V, and slightly increased for EABs poised at +0.2 V (although the corresponding standard deviation is larger, resulting in less confidence) and at potentials ≤ −0.35 V (Fig. 4). At the end of the experiment, it reached a maximum at −0.35 V [(2.4 ± 0.2) nmol cm^{-2} s$^{-1/2}$] followed by −0.4 V [1.1 nmol cm^{-2} s$^{-1/2}$) and −0.3 V [(0.90 ± 0.5) nmol cm^{-2} s$^{-1/2}$]. This result further suggests that growth at so-called "suboptimal potentials" (i.e. below plateau potentials) but ≤ $E_{1/2}$ (i.e. −0.35 V) develop more conductive and efficient EABs, though in a slower fashion.

3.4. Morphology and volume of EABs

At the end of the experiment, the morphology of EABs was recorded by confocal microscopy (Fig S12). Fluorescence images confirm that no EAB developed on electrodes poised at −0.45 V. On other electrodes that produced current, biofilms covered a slightly larger area than the 0.5 × 0.5 mm^2 gold square and exhibited a rather flat top layer (Fig. 5a). The average thickness (i.e. the volume) of the EABs showed some variations (Fig. 5b). Reliability of data for EAB poised at −0.1 V and +0.1 V is limited because of failure of the staining procedure. Biofilms grown at −0.3 V, −0.25 V, −0.2 V, −0.15 V and 0 V had similar volume of (1.22 ± 0.14) × 10^{-2} mm^3, whereas EABs polarized at −0.4 V (1 × 10^{-3} mm^3) and +0.2 V [(2.0 ± 0.5) × 10^{-3} mm^3] had a much lower volume which correlates with their lower recorded current densities. Finally, EABs that developed at −0.35 V exhibited considerably lower volumes [(1.7 ± 2.6) × 10^{-3} mm^3, n = 3] than other EABs that delivered similar maximum current densities (Fig. S14 shows the evolution of the catalytic current per EAB volume). This results seems in good adequation with the facts that (i) those EABs grown at $E_{1/2}$ had a much higher charge transport parameter than their counterparts grown at higher potentials (Fig. 4), i.e. that those more conductive EABs may be able to deliver more current per volume of biomass, and (ii) their catalytic current was still substantially increasing between t = 200 h and t = 250 h while the currents from other EABs were stable or already decreasing, suggesting that EABs were still considerably growing until acetate started to be depleted. As such, one may conjecture that the volume and the electrochemical performance of those EABs grown at $E_{1/2}$ could have increased further if a third growth cycle would have been carried out.

4. Conclusions

Here we showed that acetate-fed EABs grow the fastest and exhibit very similar electrochemical performances on electrodes polarized within the anodic plateau (−0.2 V to +0.1 V vs. Ag/AgCl) until +0.2 V vs. Ag/AgCl, at which point growth and current production were inhibited. Poising electrodes at lower potentials surrounding the apparent $E_{1/2}$ of the redox protein(s) performing the DET (−0.35 V) induced slower growth but produced EABs generating a higher current density and exhibiting better ability for electron transport.

In a wider context, we demonstrated the benefit of a high-throughput, affordable potentiostat with 128 individual channels for carrying out rigorous investigations in the field of electromicrobiology. This setup could alleviate the recurrent limitation in data points and replicates numbers for performing a broad range of studies, such as: (i) optimization of the electric input applied to electrodes to maximize growth, current production or select for a community within EABs; (ii) screening for electroactivity of either pure cultures or diverse inocula over a broad range of potentials simultaneously spanning both cathodic and anodic putative DET, and (iii) fundamental studies relative to extracellular electron transfer mechanisms, associated thermodynamics and growth yield.

Further production process optimization is necessary for increasing the yield, i.e. the ratio of correctly functioning electrodes compared to the total number of electrodes, of the 128-electrode array. Moreover, high-throughput recordings bring along the collection of vast datasets making manual analyses impractical. It is therefore essential to develop *ad hoc* automated procedures for data processing. In its present form, the setup only allows to perform studies with a single medium and a single inoculum at a time. Further integration with lab-on-chip technologies could alleviate this constraint towards electrode arrays with individual wells.

Acknowledgments

T.M. and M.V. are been supported by the EU ERC project ReSENSE under grant agreement ERC-2016-STG-715037. A.P. and K.R. are supported by a Geconcerteerde Onderzoeksacties (GOA) research grant from Ghent University (BOF-2019-GOA-026-L). A.P. kindly thanks Lori Ann Zacharoff and Benny Korth for interesting discussions.

A. Supplementary material

The supplementary information of this work is added in a separate file.

References

Bakke, R., Olsson, P., 1986. Biofilm thickness measurements by light microscopy. J. of Microbiological Methods 5, 93–98.

Bansal, R., Helmus, R.A., Stanley, B.A., Zhu, J., Liermann, L.J., Brantley, S.L., Tien, M., 2013. Survival during long-term starvation: Global proteomics analysis of geobacter sulfurreducens under prolonged electron-acceptor limitation. J. Proteome Res. 12, 4316–4326.

Besseling, T.H., Jose, J., Van Blaaderen, A., 2015. Methods to calibrate and scale axial distances in confocal microscopy as a function of refractive index. J. Microsc. 257, 142–150.

Beyene, H.D., Werkneh, A.A., Ambaye, T.G., 2018. Current updates on waste to energy (WtE) technologies: a review. Renewable Energy Focus 24, 1–11.

Bonanni, P.S., Bradley, D.F., Schrott, G.D., Busalmen, J.P., 2013. Limitations for current production in geobacter sulfurreducens biofilms. ChemSusChem 6, 711–720.

Borole, A.P., Reguera, G., Ringeisen, B., Wang, Z.W., Feng, Y., Kim, B.H., 2011. Electroactive biofilms: Current status and future research needs. Energy Environ. Sci. 4, 4813–4834.

Bosch, J., Lee, K.Y., Hong, S.F., Harnisch, F., Schröder, U., Meckenstock, R.U., 2014. Metabolic efficiency of geobacter sulfurreducens growing on anodes with different redox potentials. Curr. Microbiol. 68, 763–768.

Busalmen, J.P., Esteve-Nuñez, A., Feliu, J.M., 2008. Whole cell electrochemistry of electricity-producing microorganisms evidence an adaptation for optimal exocellular electron transport. Environ. Sci. Technol. 42, 2445–2450.

Carmona-Martínez, A.A., Harnisch, F., Kuhlicke, U., Neu, T.R., Schröder, U., 2013. Electron transfer and biofilm formation of shewanella putrefaciens as function of anode potential. Bioelectrochemistry 93, 23–29.

Dennis, P.G., Virdis, B., Vanwonterghem, I., Hassan, A., Hugenholtz, P., Tyson, G.W., Rabaey, K., 2016. Anode potential influences the structure and function of anodic electrode and electrolyte-associated microbiomes. Sci. Rep. 6.

Dirckx, J.J., Kuypers, L.C., Decraemer, W.F., 2005. Refractive index of tissue measured with confocal microscopy. J. of Biomedical Optics 10, 1–8.

Espinoza, E.M., Clark, J.A., Soliman, J., Derr, J.B., Morales, M., Vullev, V.I., 2019. Practical aspects of cyclic voltammetry: How to estimate reduction potentials when irreversibility prevails. J. Electrochem. Soc. 166.

Ferrer, M.D., Rodriguez, J.C., Álvarez, L., Artacho, A., Royo, G., Mira, A., 2017. Effect of antibiotics on biofilm inhibition and induction measured by real-time cell analysis. J. Appl. Microbiol. 122, 640–650.

Finkelstein, D.A., Tender, L.M., Zeikus, J.G., 2006. Effect of electrode potential on electrode-reducing microbiota. Environ. Sci. Technol. 40, 6990–6995.

Guo, K., Freguia, S., Dennis, P.G., Chen, X., Donose, B.C., Keller, J., Gooding, J.J., Rabaey, K., 2013. Effects of surface charge and hydrophobicity on anodic biofilm formation, community composition, and current generation in bioelectrochemical systems. Environ. Sci. Technol. 47, 7563–7570.

Guo, K., Prévoteau, A., Rabaey, K., 2017. A novel tubular microbial electrolysis cell for high rate hydrogen production. J. of Power Sources 356, 484–490.

Hu, Y., Sharma, S., Weatherwax, J., Cass, A., Georgiou, P., 2016. A portable multi-channel potentiostat for real-time amperometric measurement of multi-electrode sensor arrays, in: 2016 IEEE Int. Sym. on Circuits and Systems (ISCAS), pp. 1306–1309.

Ishii, S., Suzuki, S., Norden-Krichmar, T.M., Phan, T., Wanger, G., Nealson, K.H., Sekiguchi, Y., Gorby, Y.A., Bretschger, O., 2014. Microbial population and functional dynamics associated with surface potential and carbon metabolism. ISME J. 8, 963–978.

Jana, P.S., Katuri, K., Kavanagh, P., Kumar, A., Leech, D., 2014. Charge transport in films of geobacter sulfurreducens on graphite electrodes as a function of film thickness. Phys. Chem. Chem. Phys. 16, 9039–9046.

Joshi, K., Chan, C.H., Bond, D.R., 2019. *Geobacter sulfurreducens* requires the inner membrane b-type c-type cytochrome cbcba for reduction of electron acceptors below -0.2 V vs. SHE, in: SIMB Annual Meeting and Exhibition 2019.

Kato, S., 2017. Influence of anode potentials on current generation and extracellular electron transfer paths of *Geobacter* species. Int. J. Mol. Sci. 18.

Katuri, K.P., Rengaraj, S., Kavanagh, P., OFlaherty, V., Leech, D., 2012. Practical aspects of cyclic voltammetry: How to estimate reduction potentials when irreversibility prevails. Langmuir 166.

Korth, B., Harnisch, F., 2019. Spotlight on the energy harvest of electroactive microorganisms: The impact of the applied anode potential. Frontiers in Microbiology 10, 1352.

Kracke, F., Vassilev, I., Krömer, J.O., 2015. Microbial electron transport and energy conservation – the foundation for optimizing bioelectrochemical systems. Frontiers in Microbiology 6.

Kumar, A., Hsu, L.H.H., Kavanagh, P., Barrière, F., Lens, P.N.L., Lapinsonnière, L., Lienhard V, J.H., Schröder, U., Jiang, X., Leech, D., 2017. The ins and outs of microorganism-electrode electron transfer reactions. Nature Reviews Chemistry 1.

Leary, D.H., Hervey, W.J., Malanoski, A.P., Wang, Z., Eddie, B.J., Tender, G.S., Vora, G.J., Tender, L.M., Lin, B., Strycharz-Glaven, S.M., 2015. Metaproteomic evidence of changes in protein expression following a change in electrode potential in a robust biocathode microbiome. Proteomics 15, 3486–3496.

Levar, C.E., Chan, C.H., Mehta-Kolte, M.G., Bond, D.R., 2014. An inner membrane cytochrome required only for reduction of high redox potential extracellular electron acceptors. mBio 5.

Levar, C.E., Hoffman, C.L., Dunshee, A.L., Toner, B.M., Bond, D.R., 2017. Redox potential as a master variable controlling pathways of metal reduction by *Geobacter sulfurreducens*. ISME J. 11, 741–752.

Linhardt, P., Kührer, S., Ball, G., Biezma, M.V., 2018. Design of a multichannel potentiostat and its application to corrosion testing of a nickel-aluminum bronze. Materials and Corrosion 69.

Logan, B.E., Hamelers, B., Rozendal, R., Schroöder, U., Keller, J., Freguia, S., Aelterman, P., Verstraete, W., Rabaey, K., 2006. Microbial fuel cells: Methodology and technology. Environ. Sci. Technol. 40, 5181–5192.

Logan, B.E., Rabaey, K., 2012. Conversion of wastes into bioelectricity and chemicals by using microbial electrochemical technologies. Science 337, 686–690.

Logan, B.E., Rossi, R., Ragab, A., Saikaly, P.E., 2019. Electroactive microorganisms in bioelectrochemical systems. Nature Reviews Microbiology 17, 307–319.

Mira, A., Buetas, E., Rosier, B., Mazurel, D., Villanueva-Castellote, A., Llena, C., Ferrer, M.D., 2019. Development of an in vitro system to study oral biofilms in real time through impedance technology: validation and potential applications. J. Oral Microbiol. 11, 640–650.

Molderez, T.R., Rabaey, K., Verhelst, M., 2020. An affordable multichannel potentiostat with 128 individual stimulation and sensing channels, in: I2MTC 2020 - IEEE Int. Instrumentation and Measurement Conf.

Molderez, T.R., Zhang, X., Rabaey, K., Verhelst, M., 2019. A current-driven six-channel potentiostat for rapid performance characterization of microbial electrolysis cells. IEEE Trans. on Instrumentation and Measurement 68, 4694–4702.

Moore, G.E., 1965. Cramming more components onto integrated circuits. Electronics 38.

Parot, S., Délia, M.L., Bergel, A., 2008. Forming electrochemically active biofilms from garden compost under chronoamperometry. Bioresource Technol. 99, 4809–4816.

Pinto, D., Coradin, T., Laberty-Robert, C., 2018. Effect of anode polarization on biofilm formation and electron transfer in *Shewanella oneidensis*/graphite felt microbial fuel cells. Bioelectrochemistry 120, 1–9.

Potter, M.C., 1910. On the difference of potential due to the vital activity of micro-organisms. Proc. Durh. Univ. Philos. Soc. 3.

Prévoteau, A., Clauwaert, P., Kerckhof, F.M., Rabaey, K., 2019. Oxygen-reducing microbial cathodes monitoring toxic shocks in tap water. Biosensors and Bioelectronics 132, 115–121.

Prévoteau, A., Rabaey, K., 2017. Electroactive biofilms for sensing: Reflections and perspectives. ACS Sens. 2, 1072–1085.

Pruna, R., Palacio, F., Baraket, A., Zine, N., Streklas, A., Bausells, J., Errachid, A., López, M., 2018. A low-cost and miniaturized potentiostat for sensing of biomolecular species such as TNF-α by electrochemical impedance spectroscopy. Biosensors and Bioelectronics 100, 533–540.

Rabaey, K., Rozendal, R.A., 2010. Microbial electrosynthesis — revisiting the electrical route for microbial production. Nature Reviews Microbiology 8, 706–716.

Ramfos, I., Vassiliadis, N., Blionas, S., Efstathiou, K., Fragoso, A., O'Sullivan, C.K., Birbas, A., 2013. A compact hybrid-multiplexed potentiostat for real-time electrochemical biosensing applications. Biosensors and Bioelectronics 47, 482–489.

Richter, H., Nevin, K.P., Jia, H., Lowy, D.A., Lovley, D.R., Tender, L.M., 2009. Cyclic voltammetry of biofilms of wild type and mutant *Geobacter sulfurreducens* on fuel cell anodes indicates possible roles of OmcB, OmcZ, type iv pili, and protons in extracellular electron transfer. Energy

Environ. Sci. 9, 506–516.
Shi, L., Dong, H., Reguera, G., Beyenal, H., Lu, A., Liu, J., Yu, H.Q., Fredrickson, J.K., 2016. Extracellular electron transfer mechanisms between microorganisms and minerals. Nature Reviews Microbiology 14, 651–662.
Snider, R.M., Strycharz-Glaven, S.M., Tsoi, S.D., Erickson, J.S., Tender, L.M., 2012. Long-range electron transport in geobacter sulfurreducens biofilms is redox gradient-driven. Proc. of the National Academy of Sciences 109, 15467–15472.
Stradolini, F., Elboshra, T., Biscontini, A., De Micheli, G., Carrara, S., 2016. Simultaneous monitoring of anesthetics and therapeutic compounds with a portable multichannel potentiostat, in: 2016 IEEE Int. Sym. on Circuits and Systems (ISCAS).
Torres, C.I., Krajmalnik-Brown, R., Parameswaran, P., Marcus, A.K., Wanger, G., Gorby, Y.A., Rittmann, B.E., 2009. Selecting anode-respiring bacteria based on anode potential: Phylogenetic, electrochemical, and microscopic characterization. Environ. Sci. Technol. 43, 9519–9524.
Vergani, M., Carminati, M., Ferrari, G., Landini, E., Caviglia, C., Heiskanen, A., Comminges, C., Zor, K., Sabourin, D., Dufva, M., Dimaki, M., Raiteri, R., Wollenberger, U., Emneus, J., Sampietro, M., 2012. Multichannel bipotentiostat integrated with a microfluidic platform for electrochemical real-time monitoring of cell cultures. IEEE Trans. on Biomedical Circuits and Systems 6, 498–507.
Virdis, B., Millo, D., Donose, B.C., Batstone, D.J., 2014. Real-time measurements of the redox states of c-type cytochromes in electroactive biofilms: A confocal resonance raman microscopy study. PLOS ONE 2, 506–516.
Wagner, R.C., Call, D.F., Logan, B.E., 2010. Optimal set anode potentials vary in bioelectrochemical systems. Environ. Sci. Technol. 44, 6036–6041.
Wang, X., Aulenta, F., Puig, S., Esteve-Núñez, A., He, Y., Mu, Y., Rabaey, K., 2020. Microbial electrochemistry for bioremediation. Environ. Sci. Ecotechnol. 1.
Wei, J., Liang, P., Cao, X., Huang, X., 2010. A new insight into potential regulation on growth and power generation of *Geobacter sulfurreducens* in microbial fuel cells based on energy viewpoint. Environ. Sci. Technol. 44, 3187–3191.
Yates, M.D., Golden, J.P., Roy, J., Strycharz-Glaven, S.M., Tsoi, S., Erickson, J.S., El-Naggar, M.Y., Calabrese Barton, S., Tender, L.M., 2015. Thermally activated long range electron transport in living biofilms. Phys. Chem. Chem. Phys. 17, 32564–32570.
Zacharoff, L., Chan, C.H., Bond, D.R., 2016. Reduction of low potential electron acceptors requires the cbcl inner membrane cytochrome of geobacter sulfurreducens. Bioelectrochemistry 107, 7–13.
Zhang, X., Philips, J., Roume, H., Guo, K., Rabaey, K., Prévoteau, A., 2017. Rapid and quantitative assessment of redox conduction across electroactive biofilms by using double potential step chronoamperometry. ChemElectroChem 4, 1026–1036.
Zhang, X., Prévoteau, A., Louro, R.O., Paquete, C.M., Rabaey, K., 2018. Periodic polarization of electroactive biofilms increases current density and charge carriers concentration while modifying biofilm structure. Biosensors and Bioelectronics 121, 183–191.
Zhang, X., Rabaey, K., Prévoteau, A., 2019. Reversible effects of periodic polarization on anodic electroactive biofilms. ChemElectroChem 6, 1921–1925.
Zhao, C., Thuo, M.M., Liu, X., 2013. A microfluidic paper-based electrochemical biosensor array for multiplexed detection of metabolic biomarkers. Sc. Technol. Adv. Mater 14, 439–448.
Zhu, Z., Yates, M.D., Hatzell, M.C., Rao, H.A., Saikaly, P.E., Logan, B.E., 2013. Microbial community composition is unaffected by anode potential. Environ. Sci. Technol. 48, 1352–1358.

A chip-based 128-channel potentiostat for high-throughput studies of bioelectrochemical systems: optimal electrode potentials for anodic biofilms

Tom R. Molderez, Antonin Prévoteau, Frederik Ceyssens, Marian Verhelst, Korneel Rabaey

January 2, 2021

Supplementary information

1 User interface of the 128-channel potentiostat

The interface of the 128-channel potentiostat is command-line based. To perform experiments, a script is written to configure the 128-channel potentiostat and perform the experiments. The code listing below shows a minimal example to perform a chronoamperometry experiment with a constant potential of +0.1 V on each channel.

```
%% Example code to set a constant potential on each channel.

%% Paths
% Location of the pot128c class which controls sending commands to and
% receiving commands from the 128-channel potentiostat.
addpath('pot128c');

%% Configuration of the 128-channel potentiostat
% Load the lowlevel settings:
%       the number of channels
%       the conversion between the channel numbering in the 128-channel
%               potentiostat and MATLAB
%       the conversion functions between binary current and voltage data,
%               and physical current and voltage data
%       the particular RE for each WE
%       the sample time
gen_config;
% Create a pot128c object (P) with a file (20190919_n1_dc_voltage_lqi_4)
% to store the results
P = Pot128c('COM4', true, false, '20190919_n1_dc_voltage_lqi_4', 1, config);
% The firmware of the 128-channel potentiostat runs in debug mode. Before
% sending commands, this firmware should be programmed on the device memory
% of the microcontroller and launched.
disp('Start pot128c code!');
pause;

%% Experiment configuration
% Enable storing the results of all channels to the file
P.enable_read_all();
% Set the output of all channels to a constant potential of +0.1 V vs. Ag/AgCl
P.set_mode_all('Potential', 0.1);
% Finally, enable all channels. After this command, all channels will get a
% potential of +0.1 V vs. Ag/AgCl. The current information is written to the
% storage file.
P.enable_output_all();
```

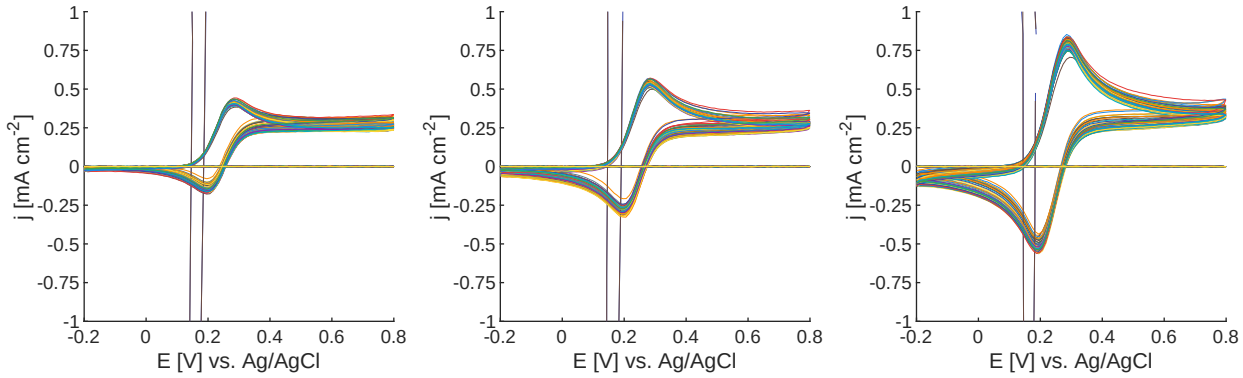

(a) (b) (c)

Figure S1: Electrochemical verification CVs (128 electrodes, third cycle) in potassium ferrocyanide for (a) $10\,\mathrm{mV\,s^{-1}}$, (b) $20\,\mathrm{mV\,s^{-1}}$, and (c) $50\,\mathrm{mV\,s^{-1}}$. Correctly manufactured electrodes (77) show a typical sigmoid response. Electrodes with a broken connection (51) show a horizontal line. Electrodes with a short connection show a vertical line.

.

2 Electrochemical verification of the 128-electrode array

To assess the correct functionality of the 128-electrode array as well as possible differences due to manufacturing, an electrochemical verification experiment was run.

2.1 Materials and methods

A square, abiotic reactor ($10\,\mathrm{cm} \times 10\,\mathrm{cm} \times 2\,\mathrm{cm}$) with 5 mM potassium ferrocyanide in 1 M NaCl at 25 °C was used. CVs were run twice with scan rates of $10\,\mathrm{mV\,s^{-1}}$, $20\,\mathrm{mV\,s^{-1}}$ and $30\,\mathrm{mV\,s^{-1}}$. The voltage range was set between $-0.2\,\mathrm{V}$ to $+0.8\,\mathrm{V}$ vs. Ag/AgCl. The current output was internally sampled at 651 Hz and next 16 × downsampled by averaging. During post-processing, the current output was further subsampled to one sample per 10 mV. The third cycle of each CV was used to verify if an electrode operated correctly.

2.2 Results and discussion

Electronic verification of the 128-electrode array was challenging because of the small dimensions (and corresponding time-intense electrode probing) in combination with the number of individual electrodes. Furthermore, the probing of an electrode resulted in a destructive scratch. Therefore, for only a few electrodes, the electrical resistance between the electrode and the connector was measured (which was in the order of $300\,\Omega$). With load currents in the range of $1\,\mu\mathrm{A}$, the resulting voltage error of $300\,\mu\mathrm{V}$ is negligible.

A second verification experiment uses ferrocyanide as a redox probe to assess the reproducibility of each electrode. The 128-electrode array was submersed in the ferrocyanide solution and equal CVs were run simultaneously on each individual electrode for different scan rates. Fig. S1 shows the third cycle of each electrode for the respective scan rates. There is a clear distinction between the voltammograms of electrodes that are manufactured correctly, which are closely matched and have a typical sigmoid response, and the voltammograms of electrodes with a manufacturing error, which either show no or almost no signal (horizontal line around 0, coinciding with the x-axis) or show the maximum current of the 128-channel potentiostat (vertical line). In the first case, a manufacturing error probably resulted in a broken (or almost broken) connection. In the second case, a short connection arose between the WE and the CE. Of the 128 electrodes, 77 operated correctly resulting in a yield of 60%. This rather low yield together with a difficult and time-intense production process forms the bottleneck for further upscaling and paralleling potentiostat channels for high-throughput experiments. These 77 verified electrodes were subsequently used for bioelectrochemical experiments. The channels of the other, non-working electrodes, were disabled using the electronic controllable switch of each channel and not further used.

3 EAB growth of the 77 channels (first and second growth cycle)

Fig. S2 shows the catalytic current density of each electrode, grouped per potential. For $-0.45\,\mathrm{V}$, 7 electrodes show no EAB growth, for $-0.4\,\mathrm{V}$, 6 electrodes show no EAB growth, for $-0.35\,\mathrm{V}$, 1 electrode shows no EAB growth, and for $+0.2\,\mathrm{V}$, 3 electrodes show no EAB growth. The internal controller of electrode 6 of $-0.3\,\mathrm{V}$ became temporally unstable at the end of the experiment causing the observed current spikes.

Fig. S3 shows the standard deviation of the catalytic current density. For most of the time and most channels, the standard deviation remains at a constant level of $\approx 0.05\,\mathrm{mA\,cm^{-2}}$. At the start of the second growth cycle, electrodes with potential $-0.1\,\mathrm{V}$ (yellow) and $+0.1\,\mathrm{V}$ (brown) show a large increase in variation probably caused by the difference in recovery rate after acetate addition. Near the end of the second growth cycle, the standard deviation increases again, probably caused by the different response on acetate depletion. Finally, the large spike of electrodes of potential $-0.3\,\mathrm{V}$ is caused by the controller of electrode 6 of that particular potential group that became unstable. For electrodes at $-0.4\,\mathrm{V}$, only one electrode showed EAB growth, thus no standard deviation could be calculated.

Fig. S4 shows the average of the accumulated charge for the 11 potentials over time. This figure highlights the difference in current increase rate and total accumulated charge.

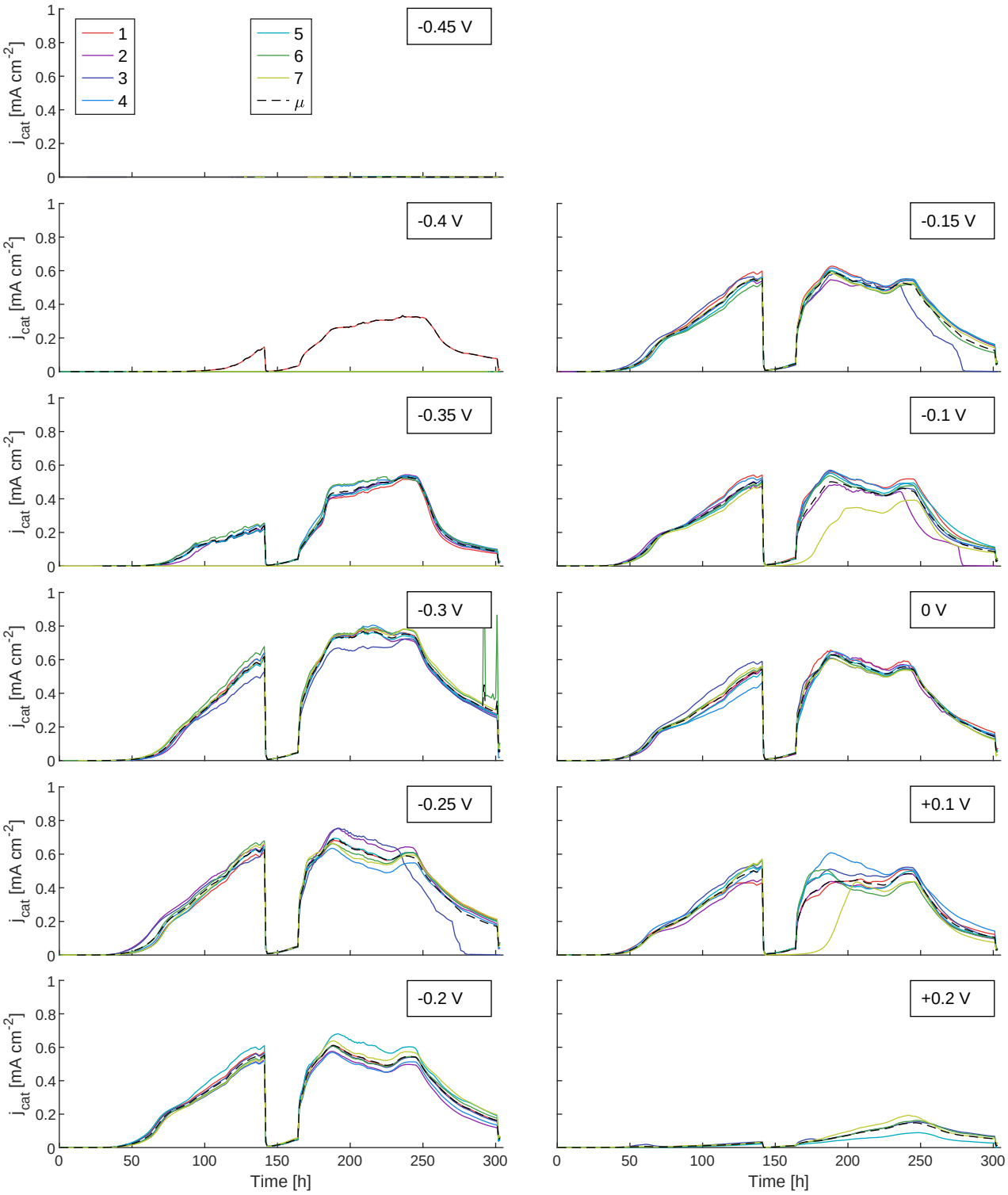

Figure S2: Catalytic current density (j_{cat}) and average (μ) of each electrode for the first and second growth cycle.

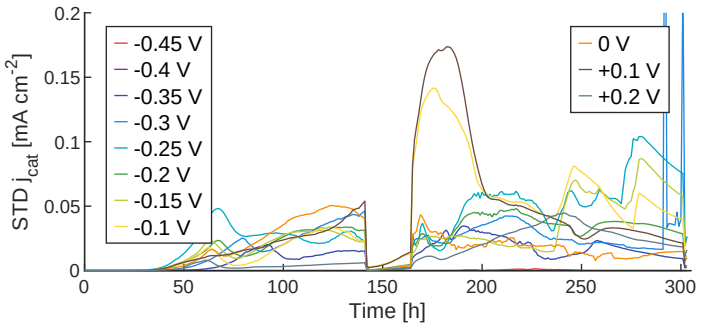

Figure S3: Standard deviation (STD) of the catalytic current density over time for the 11 different potentials (n = 7).

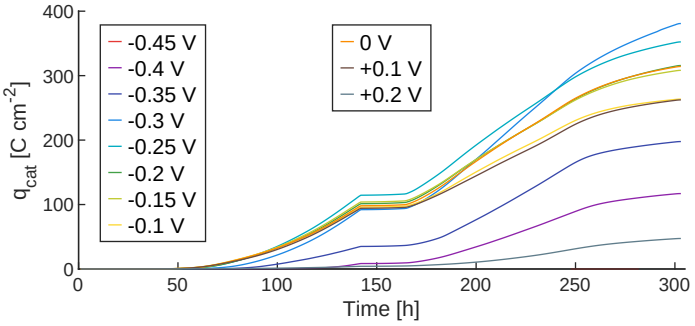

Figure S4: Average accumulated charge density for the 11 different electrode potentials over time (n = 7). The accumulated charge of electrodes poised at $-0.45\,\mathrm{V}$ is minimal and collapses with the horizontal axis.

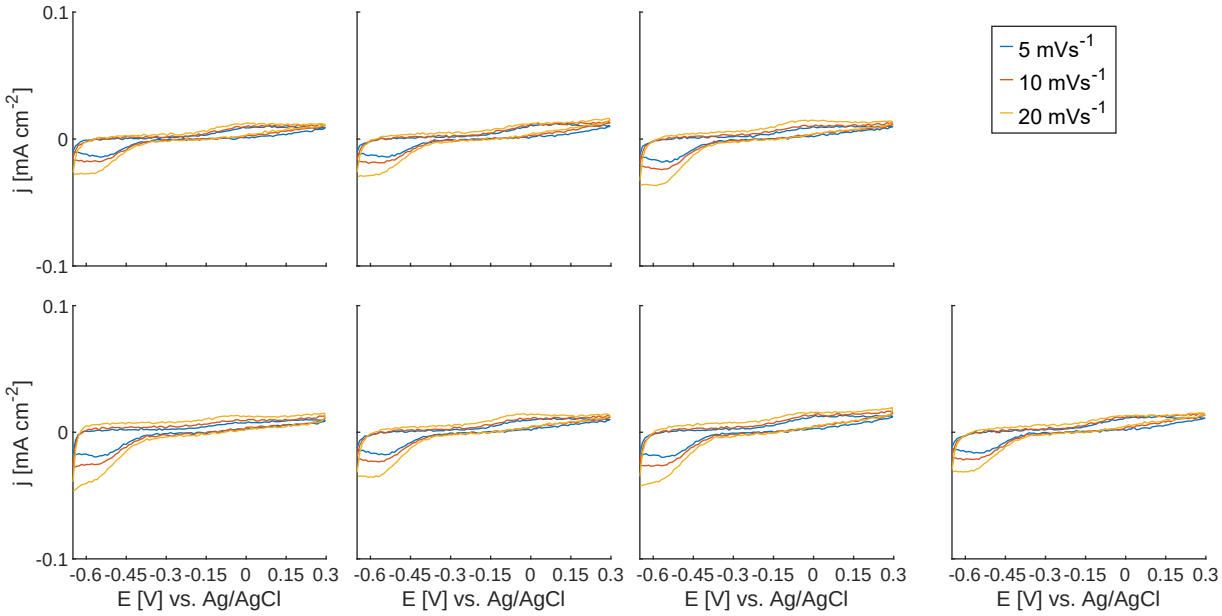

(a) −0.45 V vs. Ag/AgCl

Figure S5: Turnover CVs for (a) −0.45 V vs. Ag/AgCl after the first growth cycle for scan rates of 5 mV s^{-1} (blue), 10 mV s^{-1} (red), and 20 mV s^{-1} (yellow). Electrodes are counted first from left to right and next from top to bottom. Recorded after 142 h of polarization after inoculation.

4 Turnover CVs after the first growth cycle

Fig. S5 shows the individual 77 turnover CVs for each electrode with scan rates of 5 mV s^{-1}, 10 mV s^{-1} and 20 mV s^{-1}. Electrodes 1 to 7 of −0.45 V, electrodes 2 to 7 of −0.4 V, electrode 7 of −0.35 V, and electrode 1 to 2, and 4 of +0.2 V show no response. All other electrodes show a response typical for EABs. There is almost no difference between the different scan rates except for the expected larger overshoot near the plateau current for larger scan rates.

Fig. S6 illustrates the calculation of the midpoint potential $E_{1/2}$ for electrode 1 of −0.3 V. The forward recorded data and backward recorded data of two successive CV scans (second and third cycle for a scan rate of 20 mV s^{-1}) are first Gaussian filtered to remove the high frequency noise. Next, the derivative of each of the 4 curves is calculated and again Gaussian filtered. The apparent midpoint potential is then calculated from the average of the maximum (yellow stars) of those 4 curves.

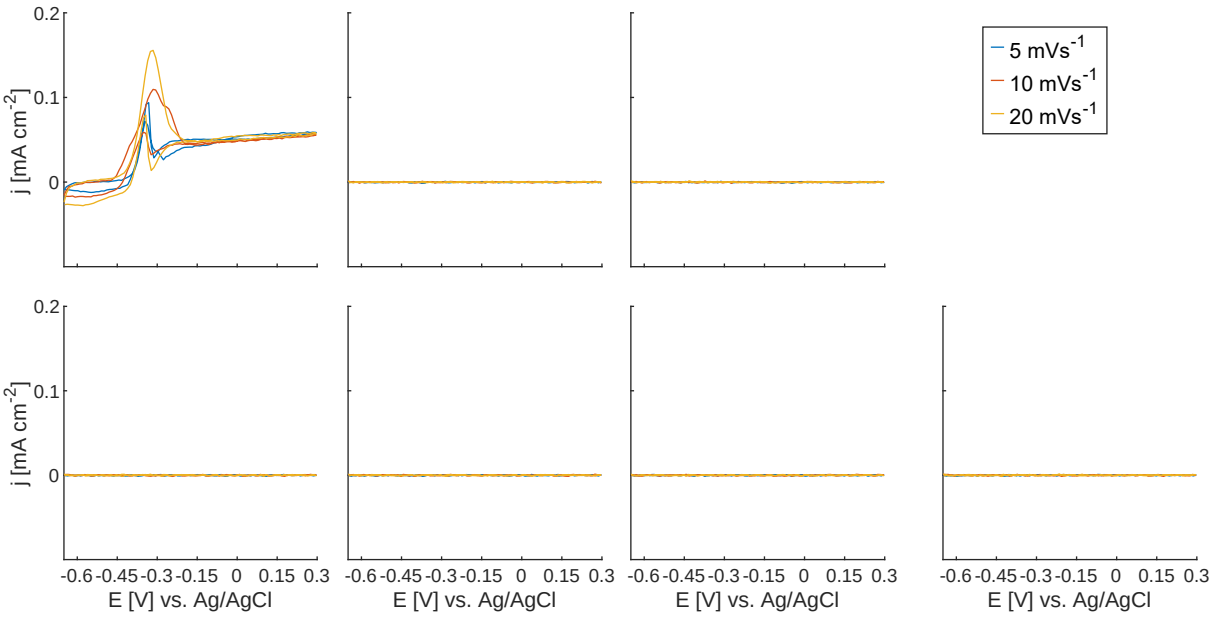

(b) −0.4 V vs. Ag/AgCl

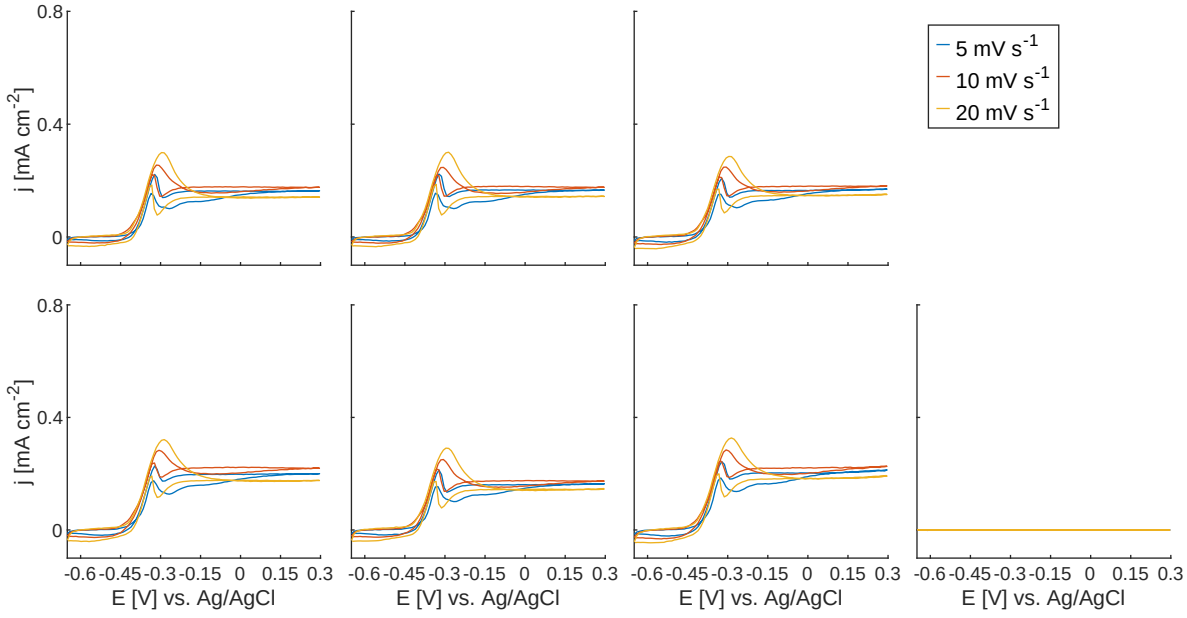

(c) −0.35 V vs. Ag/AgCl

Figure S5: (cont.) Turnover CVs for (b) −0.4 V vs. Ag/AgCl and (c) −0.35 V vs. Ag/AgCl after the first growth cycle for scan rates of 5 mV s^{-1} (blue), 10 mV s^{-1} (red), and 20 mV s^{-1} (yellow). Electrodes are counted first from left to right and next from top to bottom. Recorded after 142 h of polarization after inoculation.

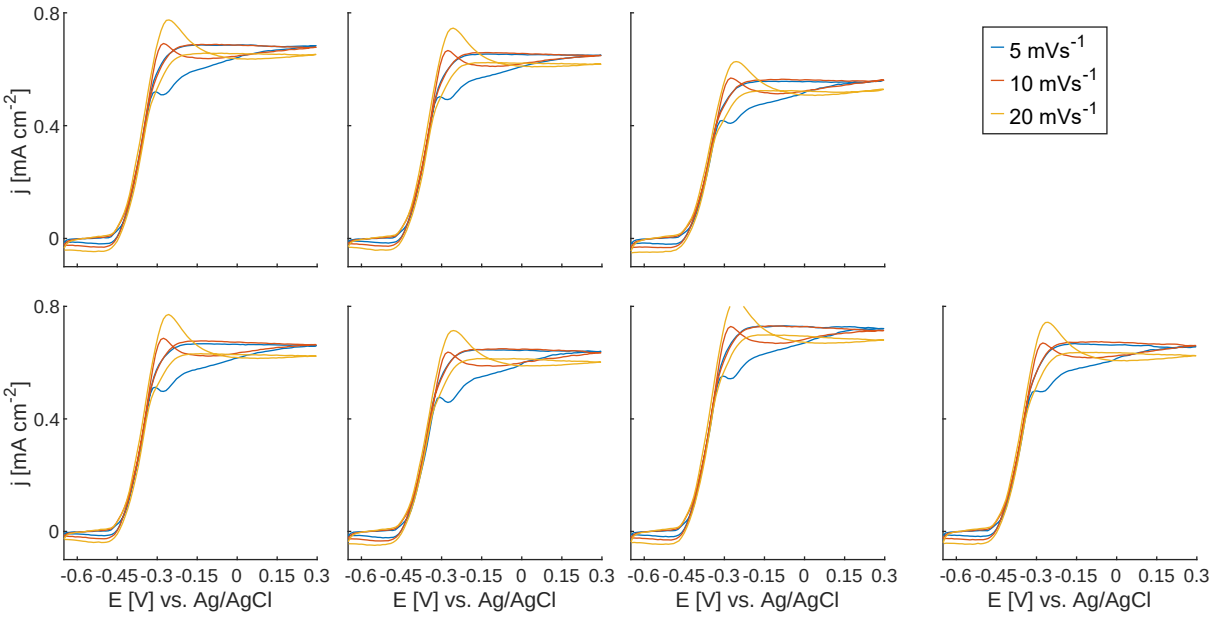

(d) −0.3 V vs. Ag/AgCl

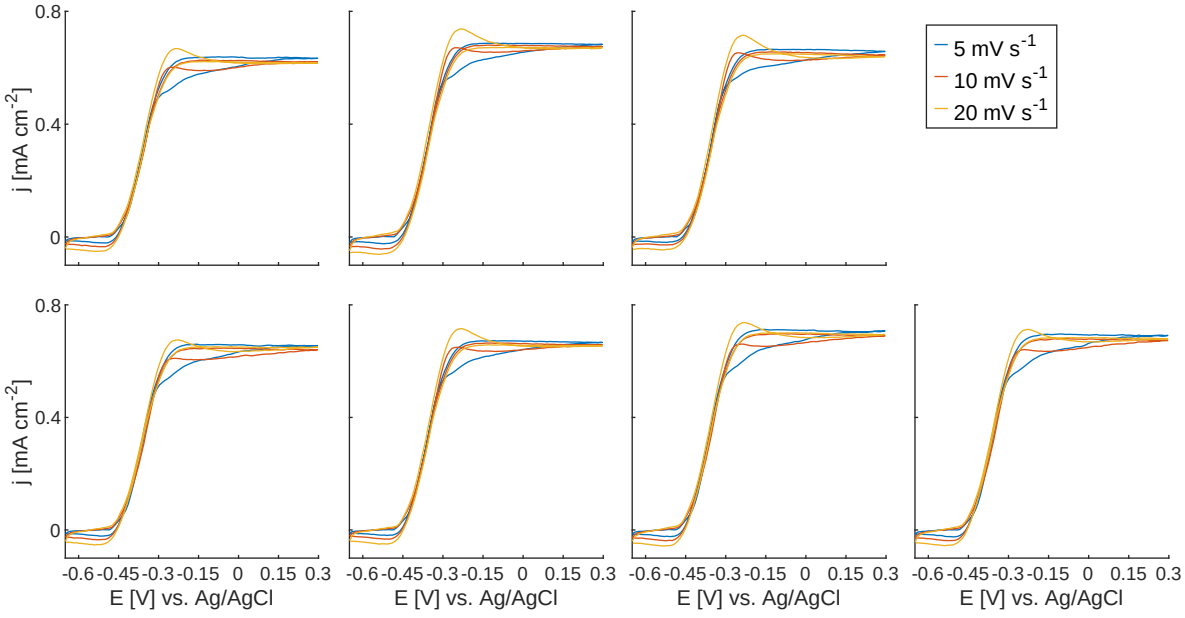

(e) −0.25 V vs. Ag/AgCl

Figure S5: (cont.) Turnover CVs for (d) −0.3 V vs. Ag/AgCl and (e) −0.25 V vs. Ag/AgCl after the first growth cycle for scan rates of 5 mV s^{-1} (blue), 10 mV s^{-1} (red), and 20 mV s^{-1} (yellow). Electrodes are counted from left to right and top to bottom. Recorded after 142 h of polarization after inoculation.

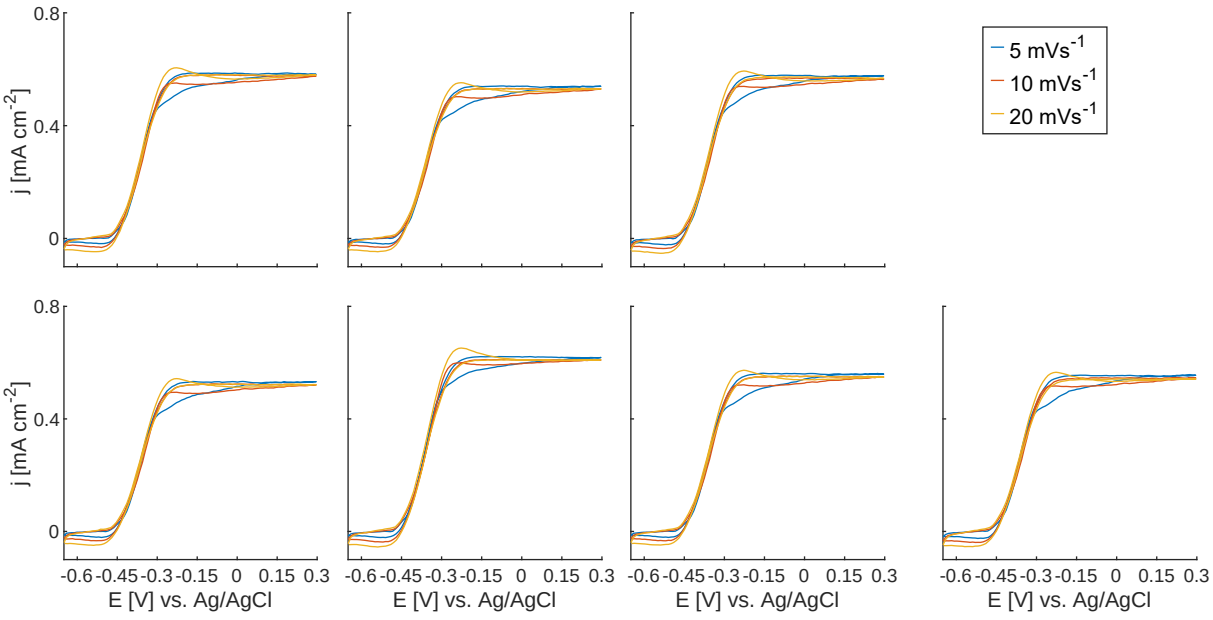

(f) −0.2 V vs. Ag/AgCl

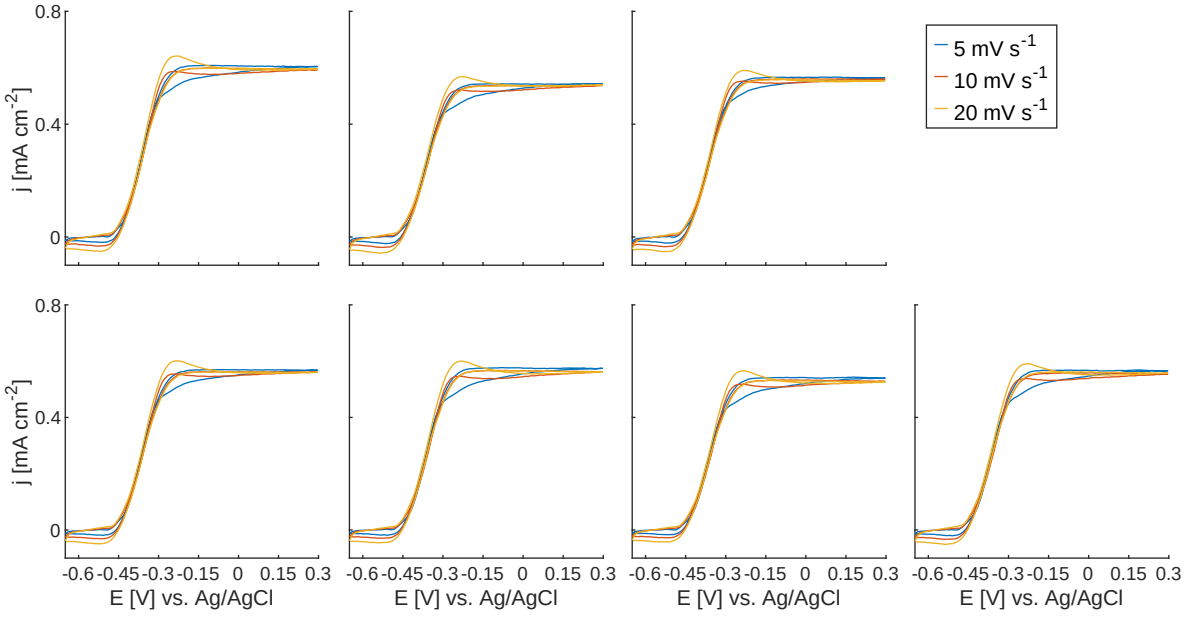

(g) −0.15 V vs. Ag/AgCl

Figure S5: (cont.) Turnover CVs for (f) −0.2 V vs. Ag/AgCl and (g) −0.15 V vs. Ag/AgCl after the first growth cycle for scan rates of 5 mV s^{-1} (blue), 10 mV s^{-1} (red), and 20 mV s^{-1} (yellow). Electrodes are counted first from left to right and next from top to bottom. Recorded after 142 h of polarization after inoculation.

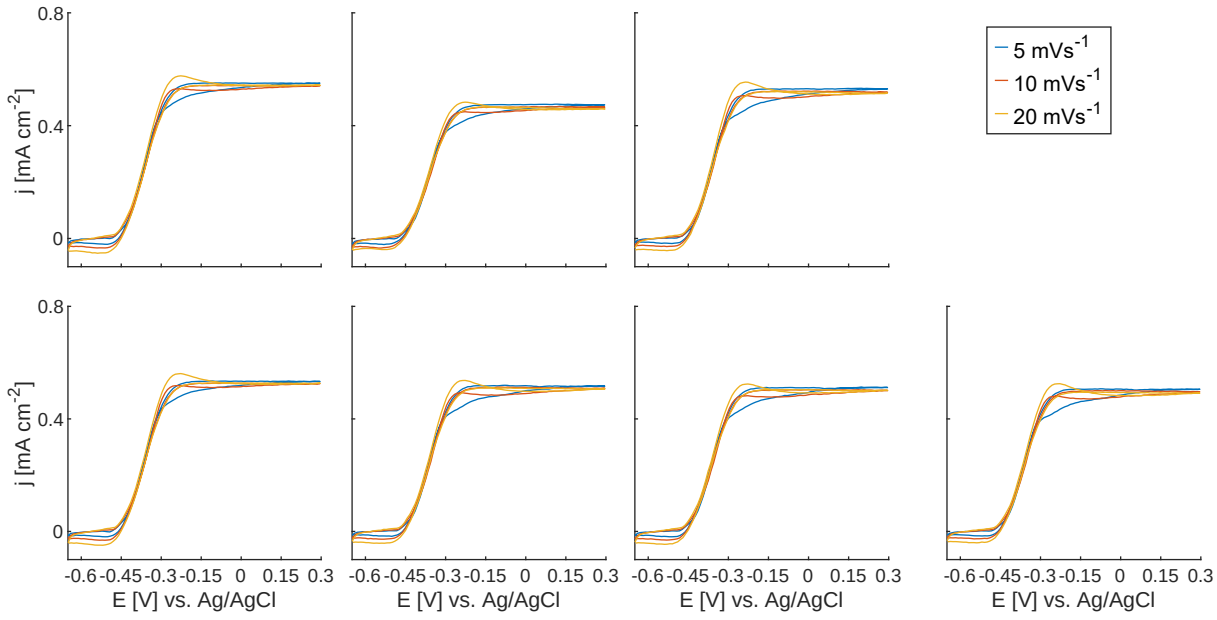

(h) −0.1 V vs. Ag/AgCl

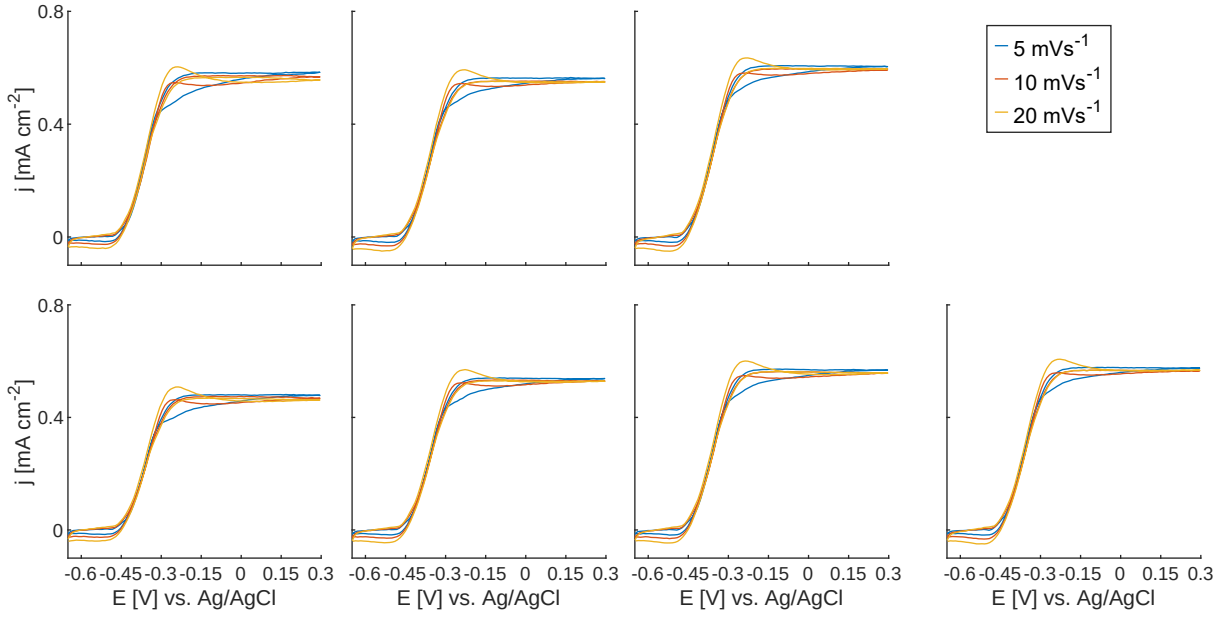

(i) 0 V vs. Ag/AgCl

Figure S5: (cont.) Turnover CVs for (h) −0.1 V vs. Ag/AgCl and (i) 0 V vs. Ag/AgCl after the first growth cycle for scan rates of 5 mV s^{-1} (blue), 10 mV s^{-1} (red), and 20 mV s^{-1} (yellow). Electrodes are counted first from left to right and next from top to bottom. Recorded after 142 h of polarization after inoculation.

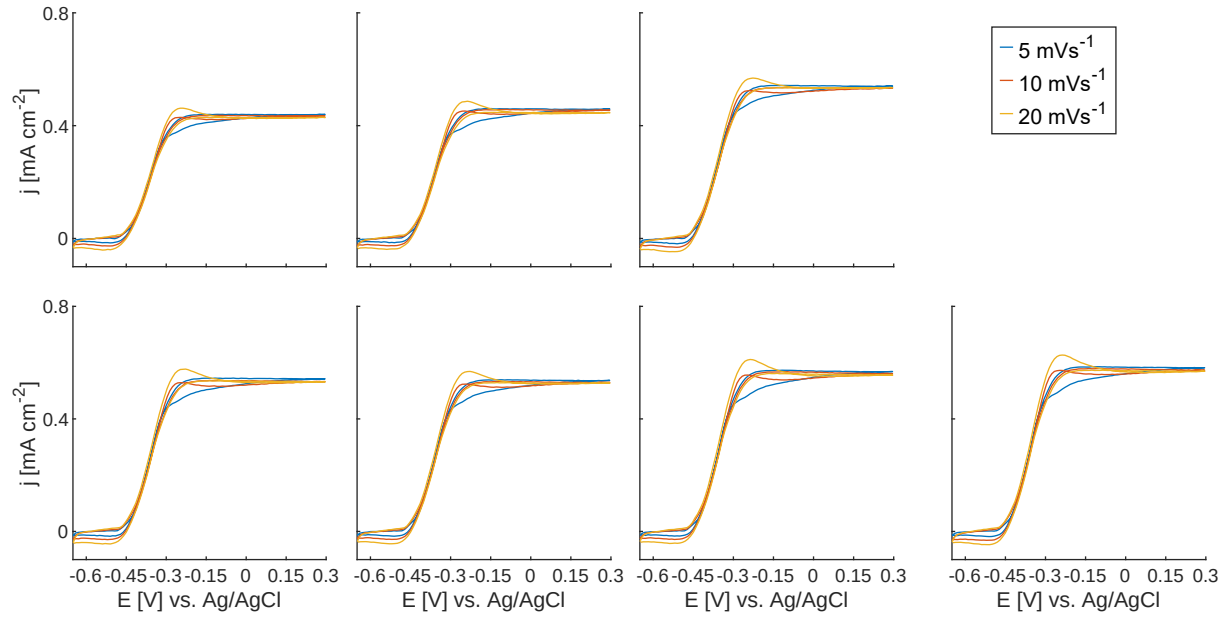

(j) +0.1 V vs. Ag/AgCl

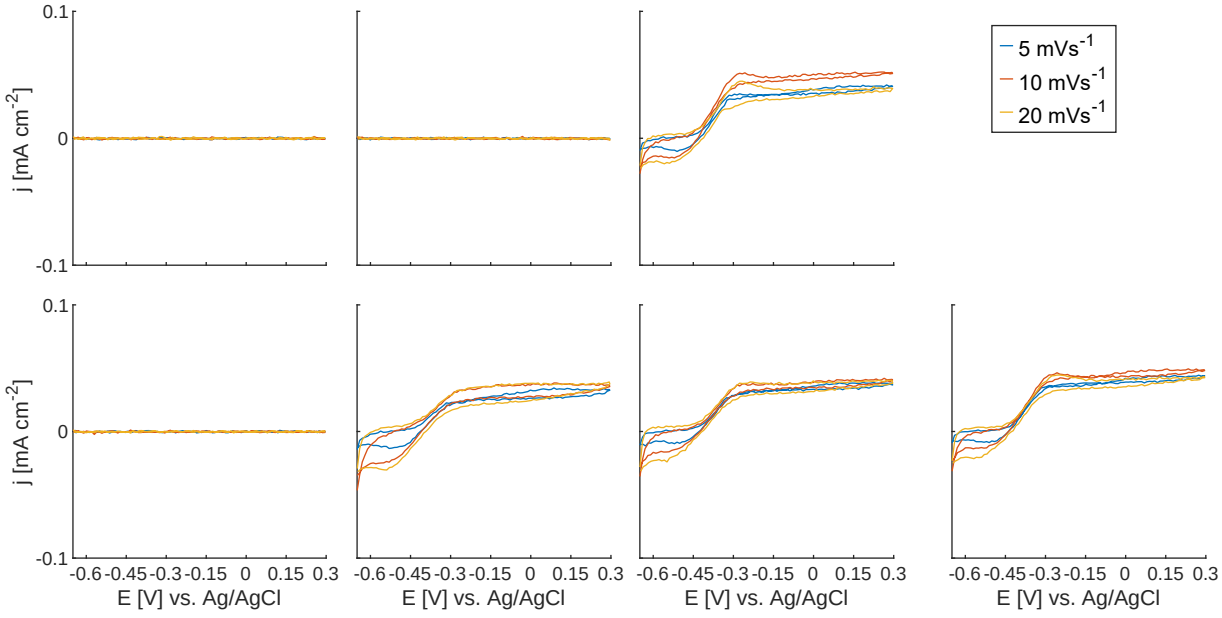

(k) +0.2 V vs. Ag/AgCl

Figure S5: (cont.) Turnover CVs for (j) +0.1 V vs. Ag/AgCl and (k) +0.2 V vs. Ag/AgCl after the first growth cycle for scan rates of 5 mV s^{-1} (blue), 10 mV s^{-1} (red), and 20 mV s^{-1} (yellow). Electrodes are counted first from left to right and next from top to bottom. Recorded after 142 h of polarization after inoculation.

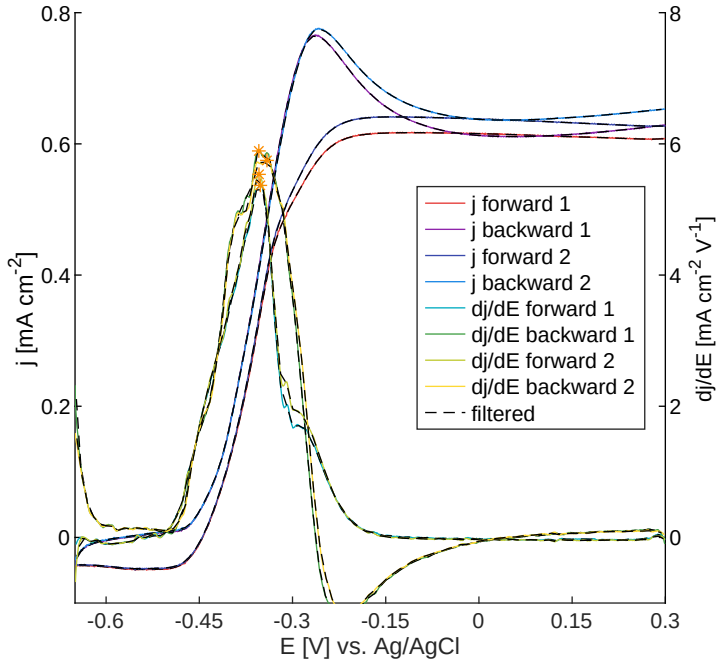

Figure S6: Illustration of the procedure used for calculating the apparent midpoint potential from a turnover CV (for electrode 1 of −0.3 V).

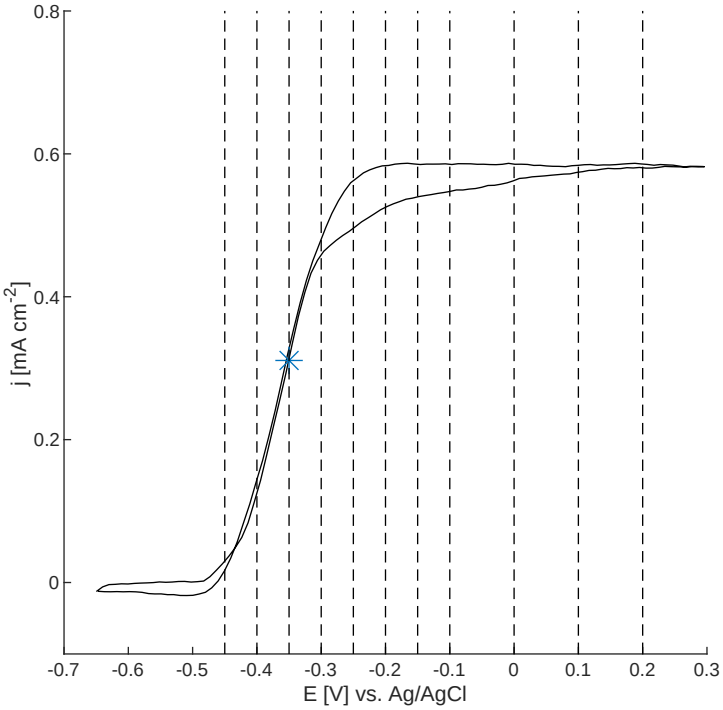

Figure S7: The black line is a representative CV of the EABs (electrode 1 with potential $-0.2\,\mathrm{V}$ vs. Ag/AgCl for a scan rate of $5\,\mathrm{mV\,s^{-1}}$. The blue star is the obtained midpoint potential $E_{1/2}$. And the dashed lines are the levels of potentials explored.

5 Set potentials motivation

Fig. S7 motivates the particular distribution of explored potentials in this study (ranging from $-0.45\,\mathrm{V}$ to $+0.2\,\mathrm{V}$ vs. Ag/AgCl). An equidistant distribution of potentials is used with a step of $0.05\,\mathrm{V}$ in the sigmoid region of the CV response and beginning of the plateau region ($-0.45\,\mathrm{V}$ to $-0.1\,\mathrm{V}$ vs. Ag/AgCl). A larger step of $0.1\,\mathrm{V}$ is used in the region of the plateau current as less variation was expected in this region ($-0.1\,\mathrm{V}$ to $+0.2\,\mathrm{V}$ vs. Ag/AgCl).

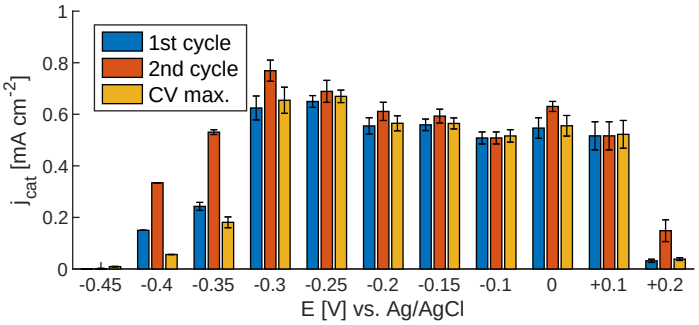

Figure S8: Maximum catalytic current density (j_{cat}) during the first growth cycle (blue), the second growth cycle (red), and extracted from the turnover CVs (yellow) (n = 7).

6 Maximum current density for the 11 different potentials

Fig. S8 compares the maximum catalytic current density (average and standard deviation) of the first and second growth cycle with the maximum current density extracted from the turnover CVs. It was expected that, especially for lower poised electrodes, the CV current density would be significantly larger than the maximum current density at the respective electrode potential for the first growth cycle. The CV current density, however, is significantly lower for anode potentials of $-0.45\,\mathrm{V}$ and $-0.4\,\mathrm{V}$ and only slightly larger for anode potentials from $-0.3\,\mathrm{V}$ to $+0.2\,\mathrm{V}$. Only one sample showed EAB growth for $-0.4\,\mathrm{V}$, explaining the lack of a standard deviation.

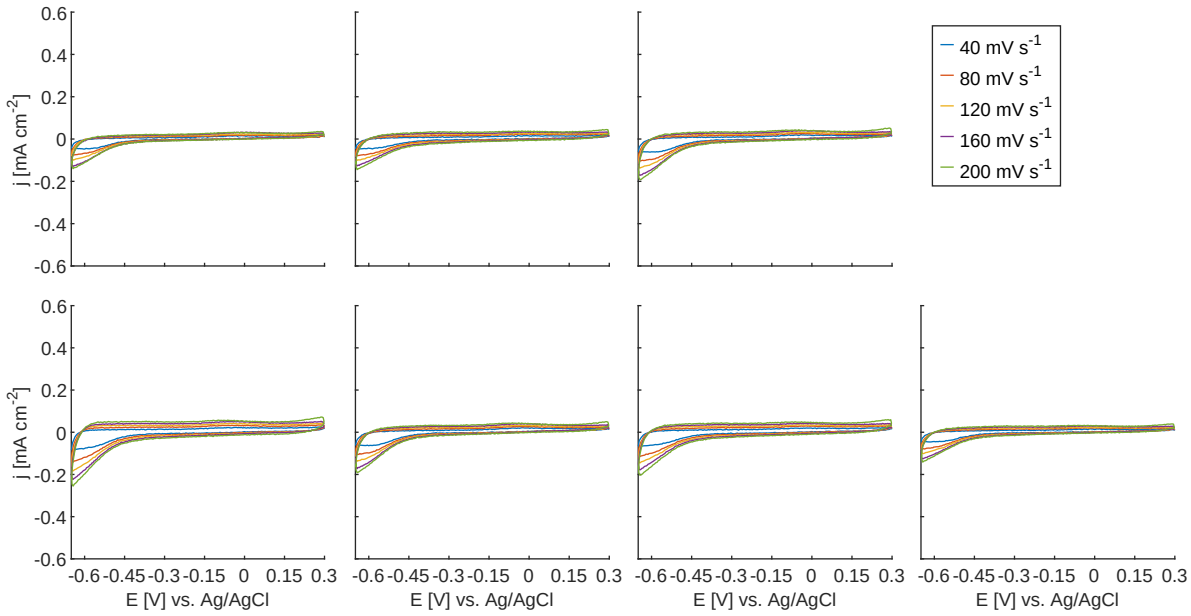

(a) −0.45 V vs. Ag/AgCl

Figure S9: Nonturnover CVs for (a) −0.45 V vs. Ag/AgCl after the first growth cycle for scan rates of 40 mV s^{-1} (blue), 80 mV s^{-1} (red), 120 mV s^{-1} (yellow), 160 mV s^{-1} (purple), and 200 mV s^{-1} (green). Electrodes are counted first from left to right and next from top to bottom. Recorded after 164 h of polarization after inoculation.

7 Nonturnover CVs after the first growth cycle

Fig. S9 shows the individual 77 nonturnover CVs for each electrode after 164 h with scan rates of 40 mV s^{-1} (blue), 80 mV s^{-1} (red), 120 mV s^{-1} (yellow), 160 mV s^{-1} (purple), and 200 mV s^{-1} (green). The CVs with scan rate of 10 mV s^{-1}, 20 mV s^{-1}, 60 mV s^{-1}, 100 mV s^{-1}, 140 mV s^{-1} and 180 mV s^{-1} are not shown to keep the figures readable. This data is nonetheless used for analysis. Electrodes 1 to 7 of −0.45 V, electrodes 2 to 7 of −0.4 V, electrode 7 of −0.35 V, electrode 7 of −0.1 V, electrode 7 of +0.1 V and electrodes 1, 2, and 4 of +0.2 V show no response. All other electrodes show a response typical for EABs. As the scan rate increases, the maximum current scales quadratic, as predicted by the Randles-Ševčík equation.

Fig. S10 illustrates the calculation of the charge transport parameter $CD_{app}^{1/2}$ using the Randles-Ševčík equation. First, the maximum current is extracted for all forward cycles of all CVs of each electrode. From this current, the background current, taken as the average current in the potential range of +0.2 V to +0.3 V, is subtracted. The current is then averaged for the multiple cycles and linear regression is applied to estimate the charge transport parameter.

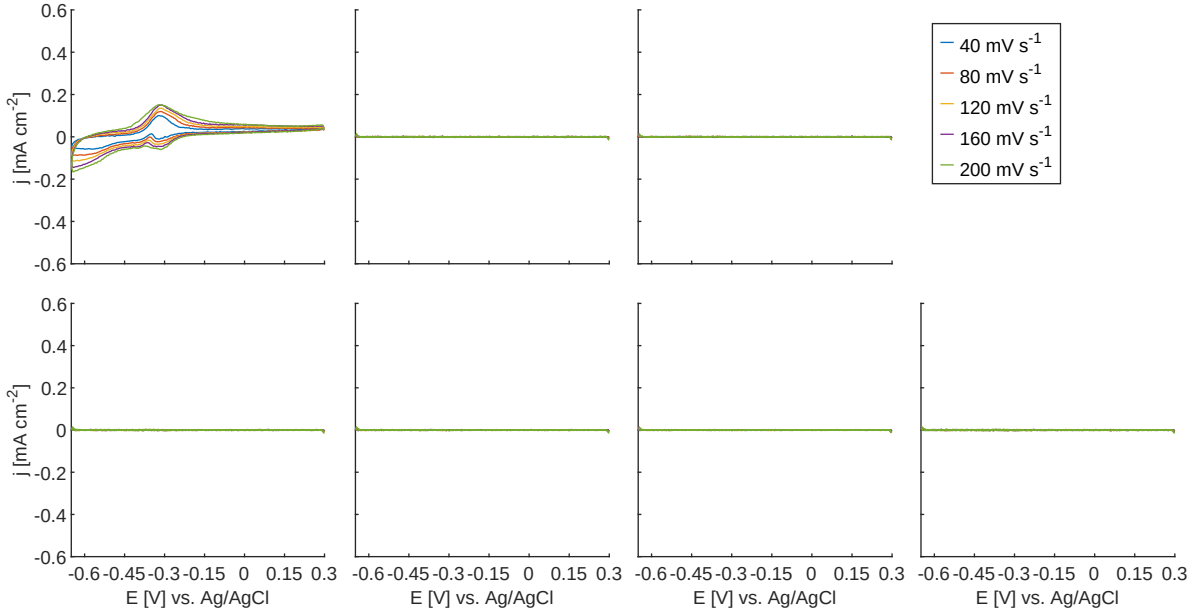

(b) −0.4 V vs. Ag/AgCl

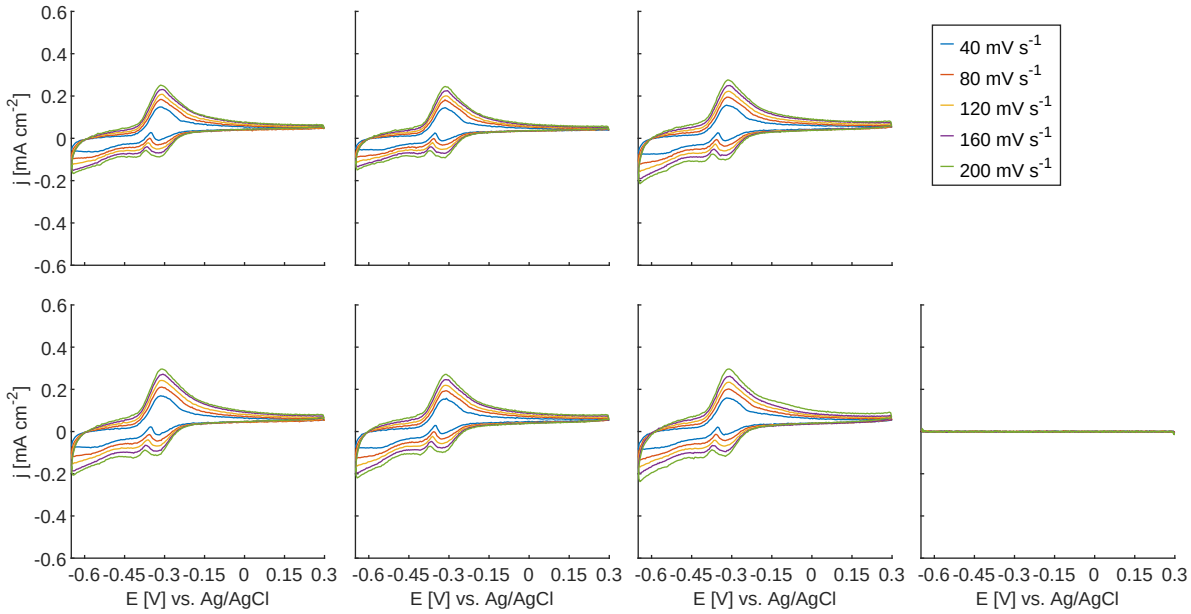

(c) −0.35 V vs. Ag/AgCl

Figure S9: (cont.) Nonturnover CVs for (b) −0.4 V vs. Ag/AgCl and (c) −0.35 V vs. Ag/AgCl after the first growth cycle for scan rates of 40 mV s^{-1} (blue), 80 mV s^{-1} (red), 120 mV s^{-1} (yellow), 160 mV s^{-1} (purple), and 200 mV s^{-1} (green). Electrodes are counted first from left to right and next from top to bottom. Recorded after 164 h of polarization after inoculation.

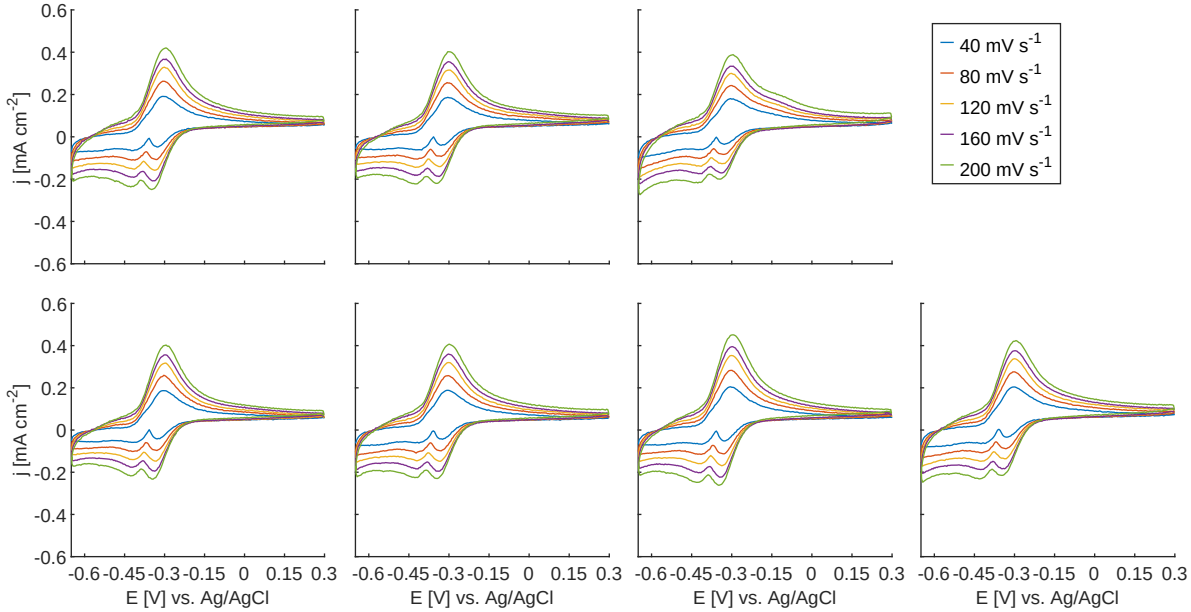

(d) −0.3 V vs. Ag/AgCl

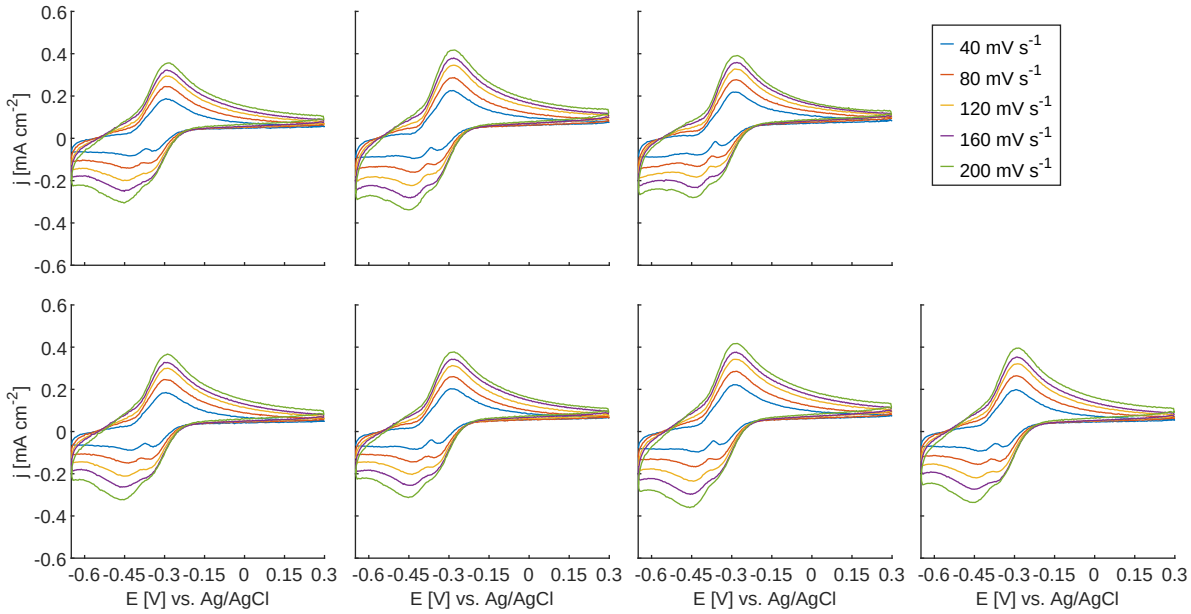

(e) −0.25 V vs. Ag/AgCl

Figure S9: (cont.) Nonturnover CVs for (d) −0.3 V vs. Ag/AgCl and (e) −0.25 V vs. Ag/AgCl after the first growth cycle for scan rates of 40 mV s^{-1} (blue), 80 mV s^{-1} (red), 120 mV s^{-1} (yellow), 160 mV s^{-1} (purple), and 200 mV s^{-1} (green). Electrodes are counted first from left to right and next from top to bottom. Recorded after 164 h of polarization after inoculation.

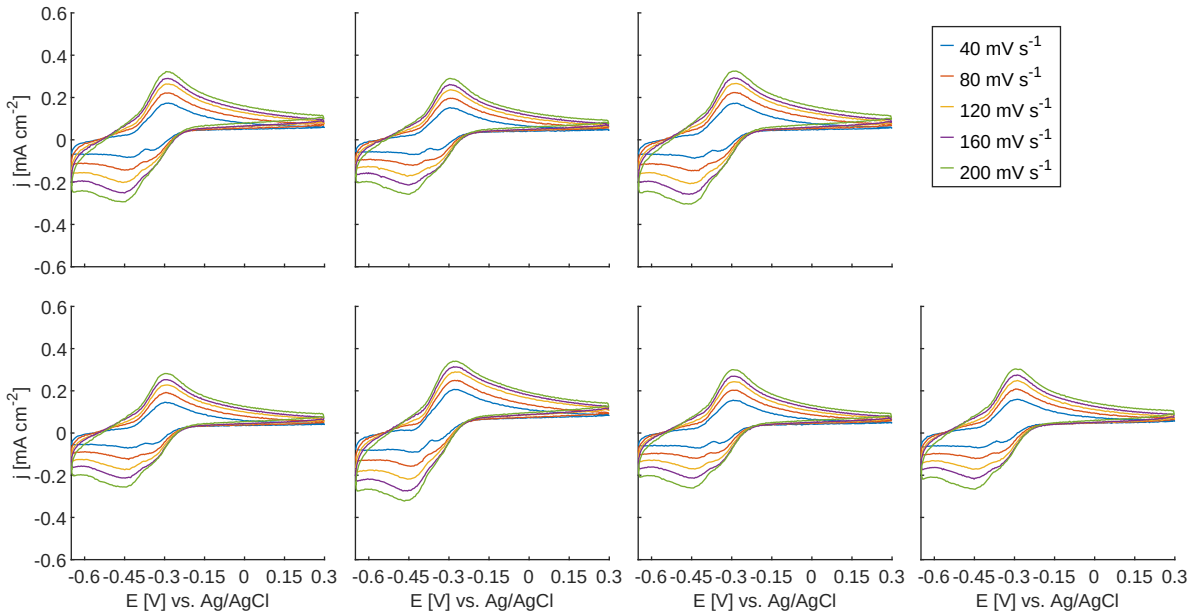

(f) −0.2 V vs. Ag/AgCl

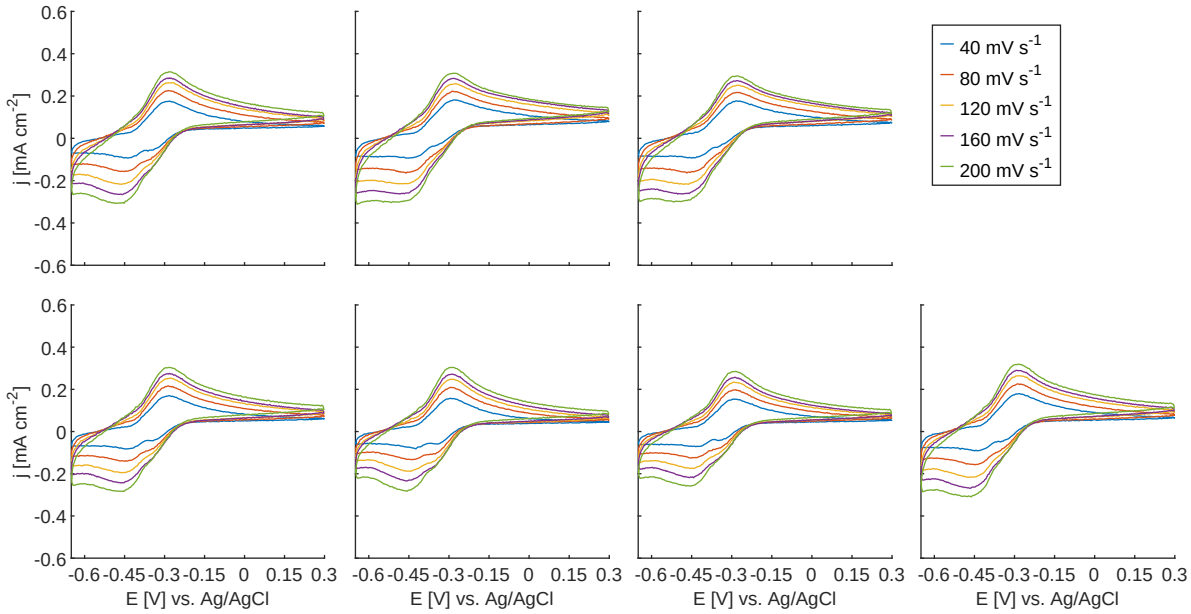

(g) −0.15 V vs. Ag/AgCl

Figure S9: (cont.) Nonturnover CVs for (f) −0.2 V vs. Ag/AgCl and (g) −0.15 V vs. Ag/AgCl after the first growth cycle for scan rates of 40 mV s^{-1} (blue), 80 mV s^{-1} (red), 120 mV s^{-1} (yellow), 160 mV s^{-1} (purple), and 200 mV s^{-1} (green). Electrodes are counted first from left to right and next from top to bottom. Recorded after 164 h of polarization after inoculation.

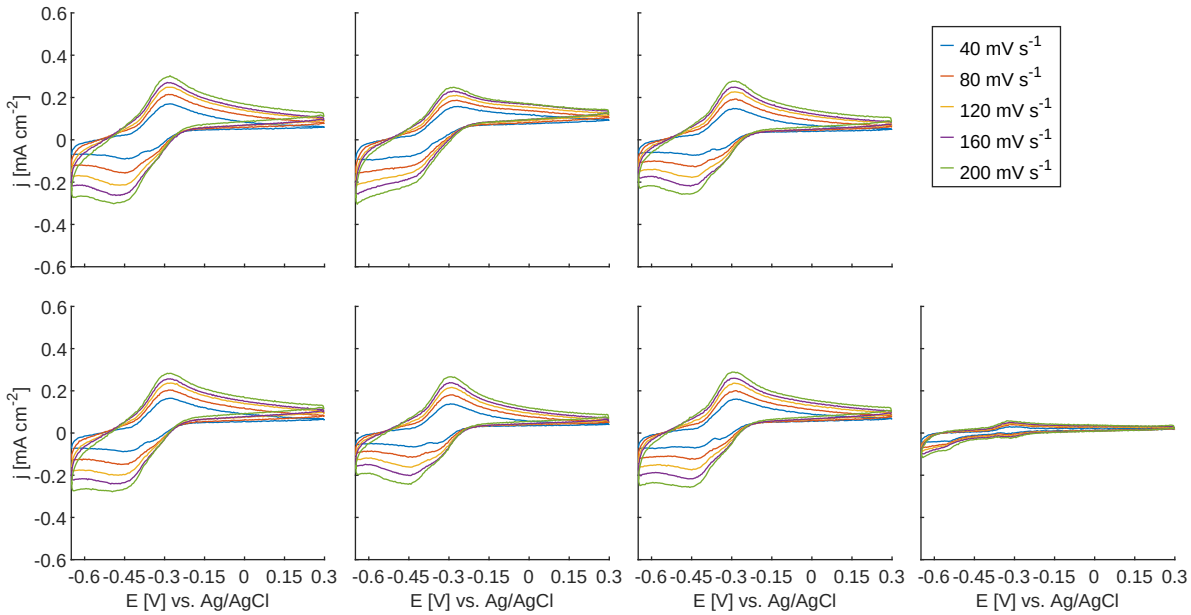

(h) −0.1 V vs. Ag/AgCl

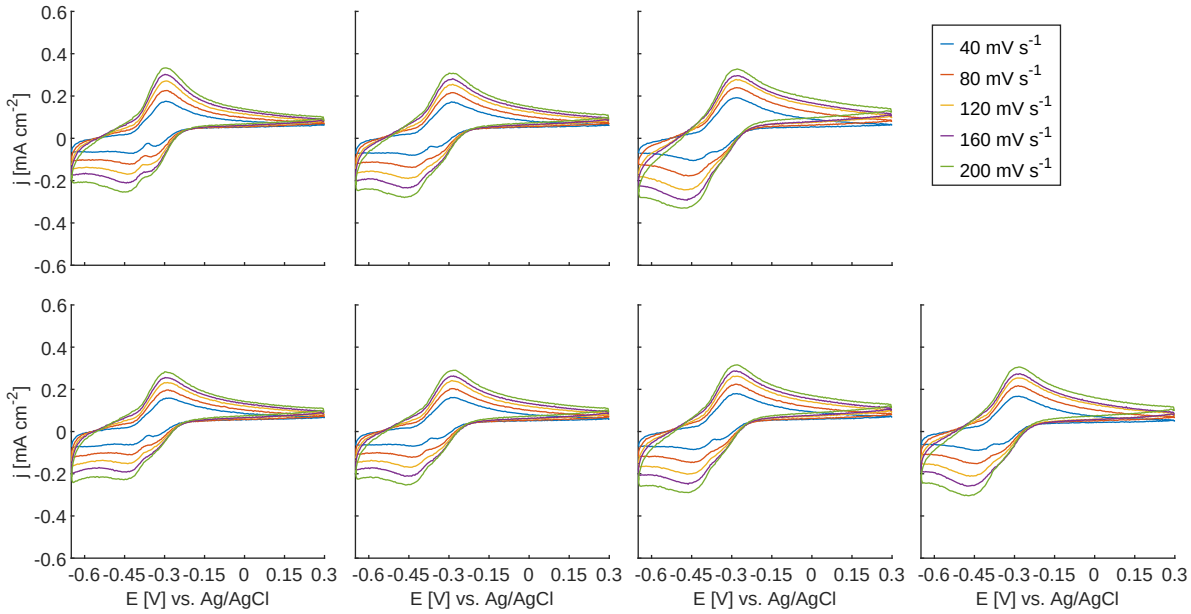

(i) 0 V vs. Ag/AgCl

Figure S9: (cont.) Nonturnover CVs for (h) −0.1 V vs. Ag/AgCl and (i) 0 V vs. Ag/AgCl after the first growth cycle for scan rates of 40 mV s^{-1} (blue), 80 mV s^{-1} (red), 120 mV s^{-1} (yellow), 160 mV s^{-1} (purple), and 200 mV s^{-1} (green). Electrodes are counted first from left to right and next from top to bottom. Recorded after 164 h of polarization after inoculation.

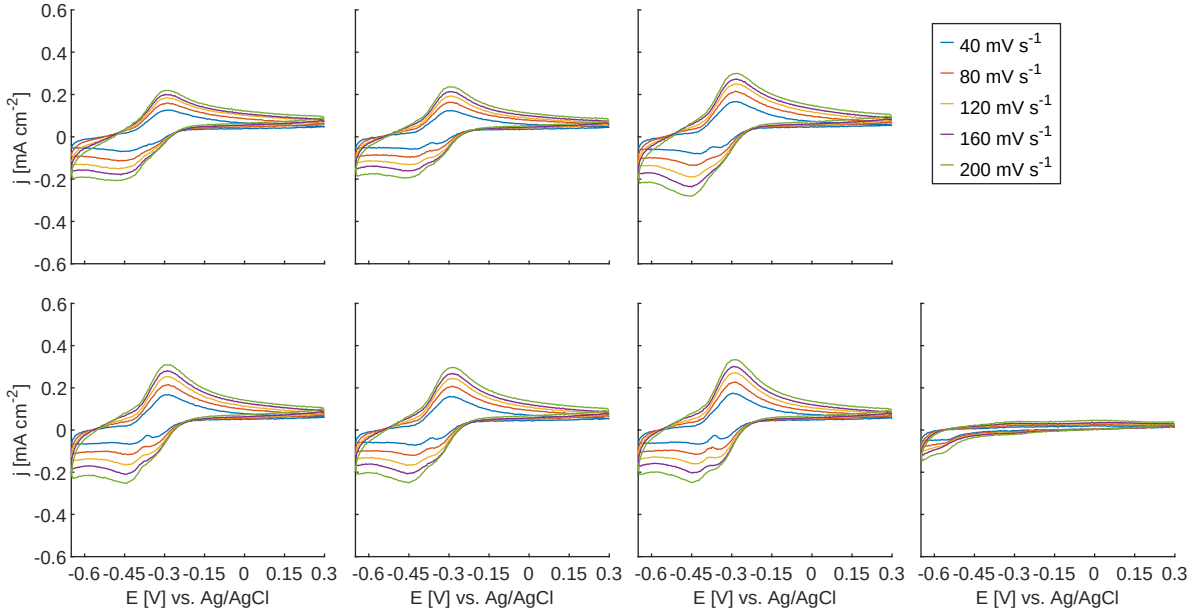

(j) +0.1 V vs. Ag/AgCl

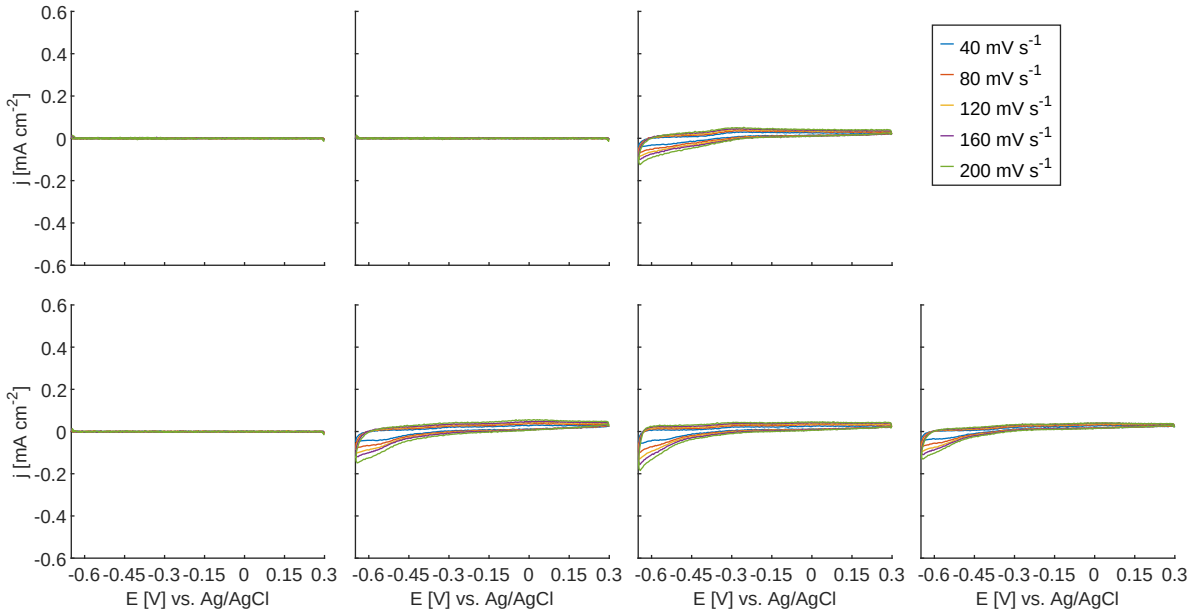

(k) +0.2 V vs. Ag/AgCl

Figure S9: (cont.) Nonturnover CVs for (j) +0.1 V vs. Ag/AgCl and (k) +0.2 V vs. Ag/AgCl after the first growth cycle for scan rates of 40 mV s^{-1} (blue), 80 mV s^{-1} (red), 120 mV s^{-1} (yellow), 160 mV s^{-1} (purple), and 200 mV s^{-1} (green). Electrodes are counted first from left to right and next from top to bottom. Recorded after 164 h of polarization after inoculation.

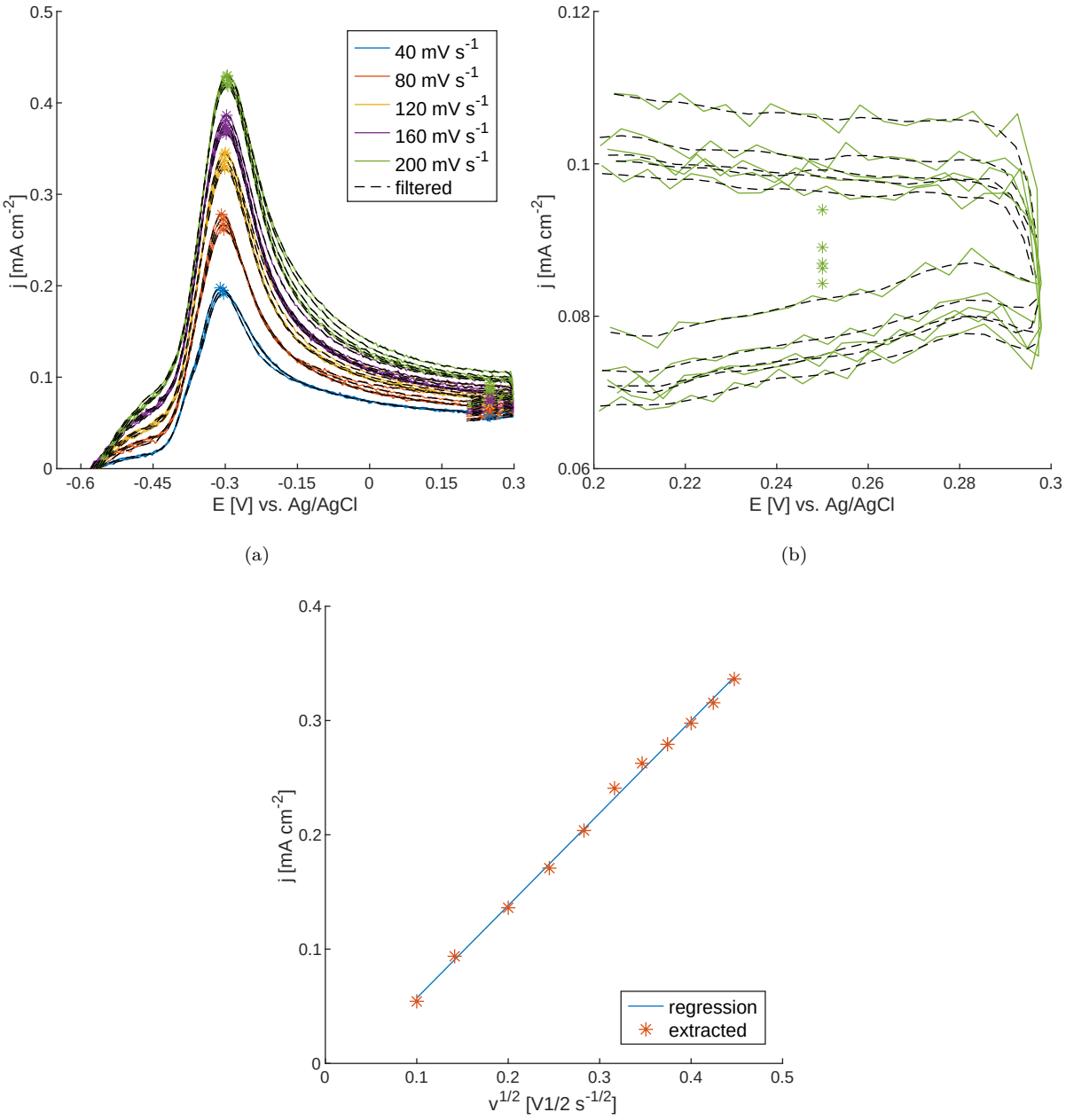

Figure S10: Illustration of the extraction of the charge transport parameter ($CD_{app}^{1/2}$) based on the Randles-Ševčík equation with (a) the maximum current for the different filtered forward CVs, (b) the background current extraction (closeup of (a)) with the stars the average current of the forward and backward CV scan at the extreme right of the CVs, taken as background currents to calculate the anodic peak currents (i.e. maximum current subtracted by the background current), and (c) the linear regression between the scan rate v (for $v^{1/2}$) and the charge transport parameter $CD_{app}^{1/2}$. This example was provided for an EAB grown at $-0.3\,\mathrm{V}$ vs. Ag/AgCl (electrode 1).

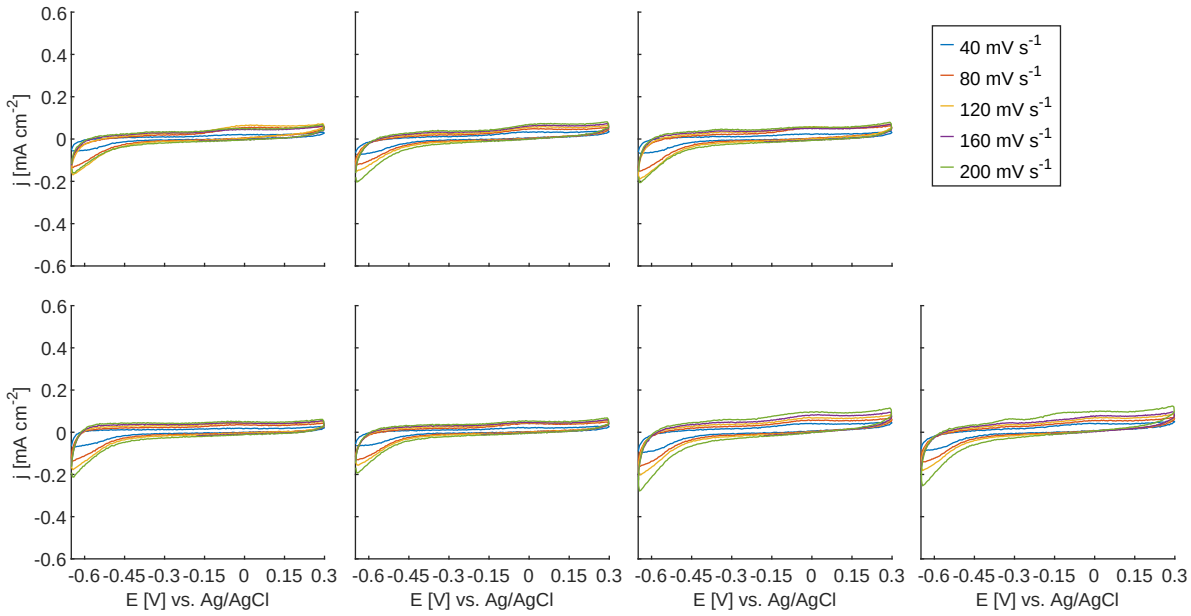

(a) −0.45 V vs. Ag/AgCl

Figure S11: Nonturnover CVs for (a) −0.45 V vs. Ag/AgCl after the second growth cycle for scan rates of 40 mV s^{-1} (blue), 80 mV s^{-1} (red), 120 mV s^{-1} (yellow), 160 mV s^{-1} (purple), and 200 mV s^{-1} (green). Electrodes are counted from left to right and top to bottom. Recorded after 324 h of polarization after inoculation.

8 Nonturnover CVs after the second growth cycle

Fig. S11 shows the individual 77 nonturnover CVs for each electrode after 324 h with scan rates of 40 mV s^{-1} (blue), 80 mV s^{-1} (red), 120 mV s^{-1} (yellow), 160 mV s^{-1} (purple), and 200 mV s^{-1} (green). The CVs with scan rate of 10 mV s^{-1}, 20 mV s^{-1}, 60 mV s^{-1}, 100 mV s^{-1}, 140 mV s^{-1} and 180 mV s^{-1} are not shown to keep the figures readable. This data is nonetheless used for analysis. Electrodes 1 to 7 of −0.45 V, electrodes 2 to 7 of −0.4 V, electrode 7 of −0.35 V, electrode 4 of −0.3 V, electrode 3 of −0.25 V, and electrodes 1, 2, and 4 of +0.2 V show no response. For electrode 6 of −0.3 V, the measurement failed. All other electrodes show a response typical for EABs. As the scan rate increases, the maximum current scales quadratically, as predicted by the Randles-Ševčík equation.

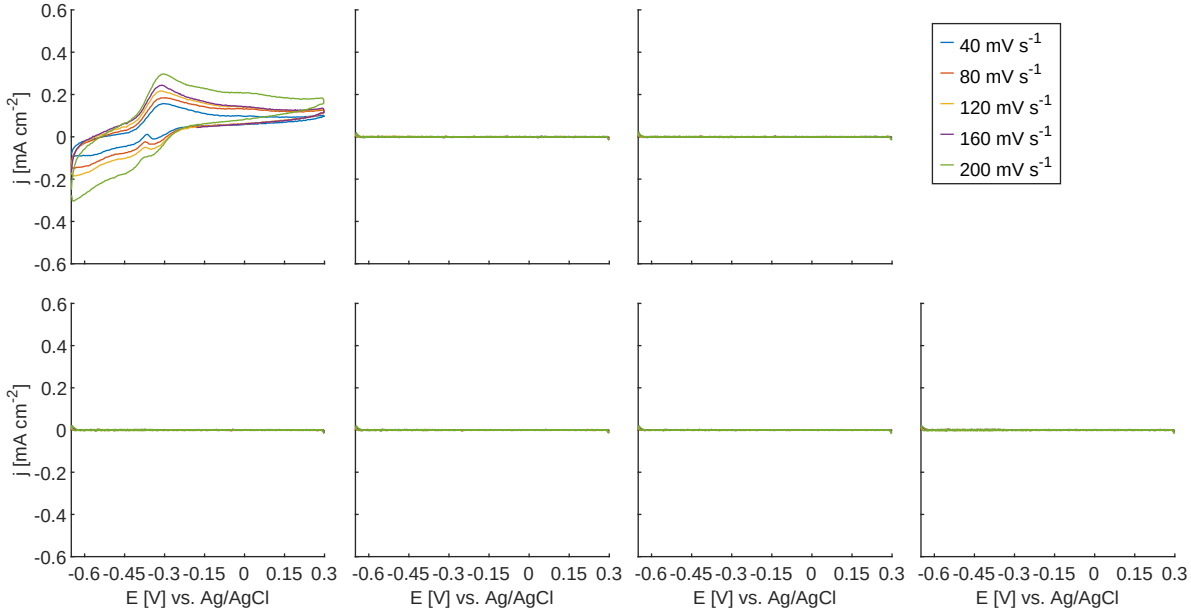

(b) −0.4 V vs. Ag/AgCl

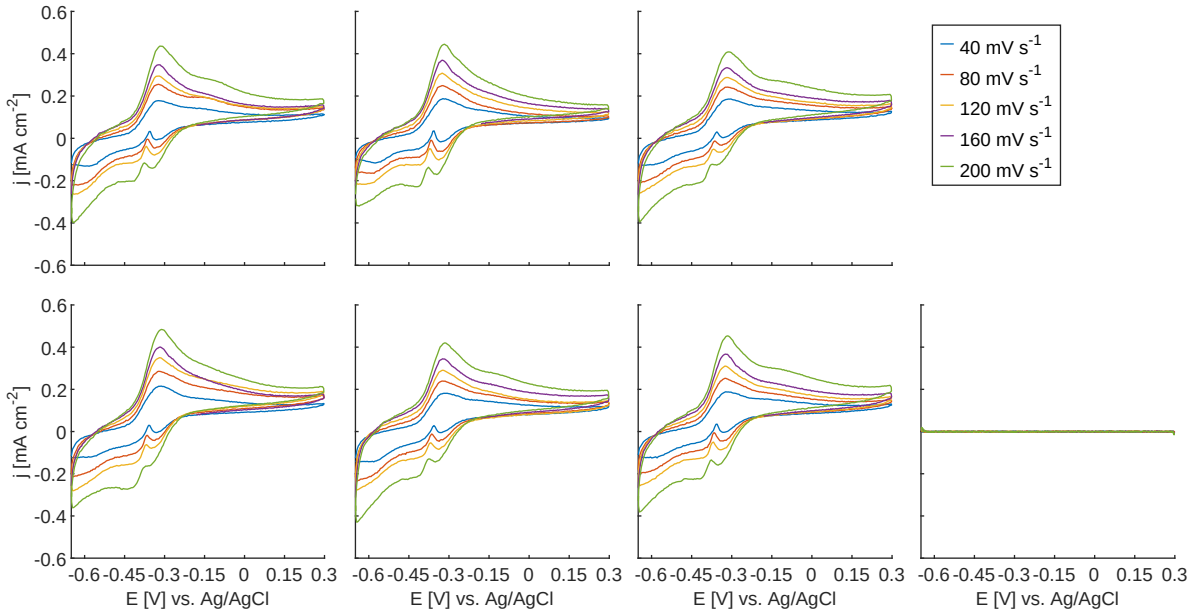

(c) −0.35 V vs. Ag/AgCl

Figure S11: (cont.) Nonturnover CVs for (b) −0.4 V vs. Ag/AgCl and (c) −0.35 V vs. Ag/AgCl after the second growth cycle for scan rates of 40 mV s^{-1} (blue), 80 mV s^{-1} (red), 120 mV s^{-1} (yellow), 160 mV s^{-1} (purple), and 200 mV s^{-1} (green). Electrodes are counted from left to right and top to bottom. Recorded after 324 h of polarization after inoculation.

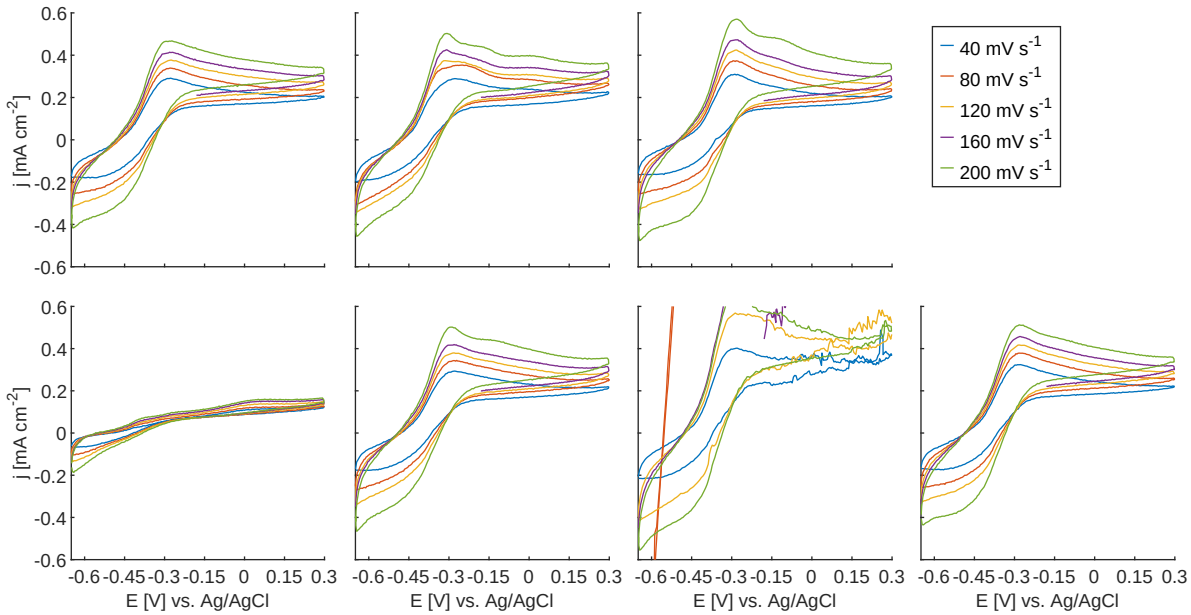

(d) −0.3 V vs. Ag/AgCl

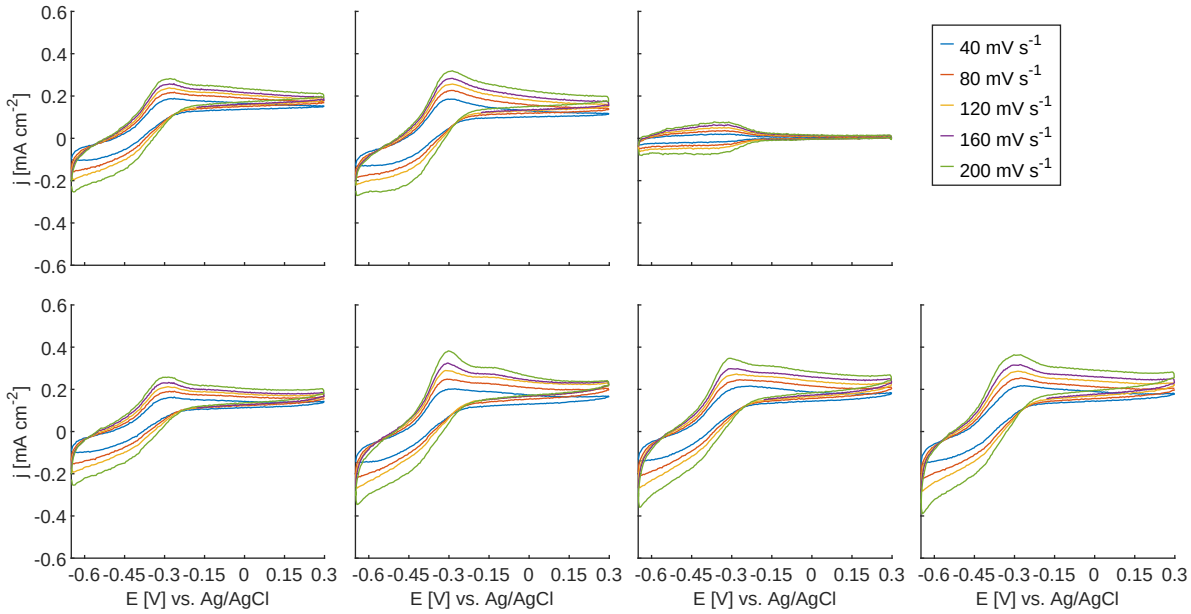

(e) −0.25 V vs. Ag/AgCl

Figure S11: (cont.) Nonturnover CVs for (d) −0.3 V vs. Ag/AgCl and (e) −0.25 V vs. Ag/AgCl after the second growth cycle for scan rates of 40 mV s^{-1} (blue), 80 mV s^{-1} (red), 120 mV s^{-1} (yellow), 160 mV s^{-1} (purple), and 200 mV s^{-1} (green). Electrodes are counted from left to right and top to bottom. Recorded after 324 h of polarization after inoculation.

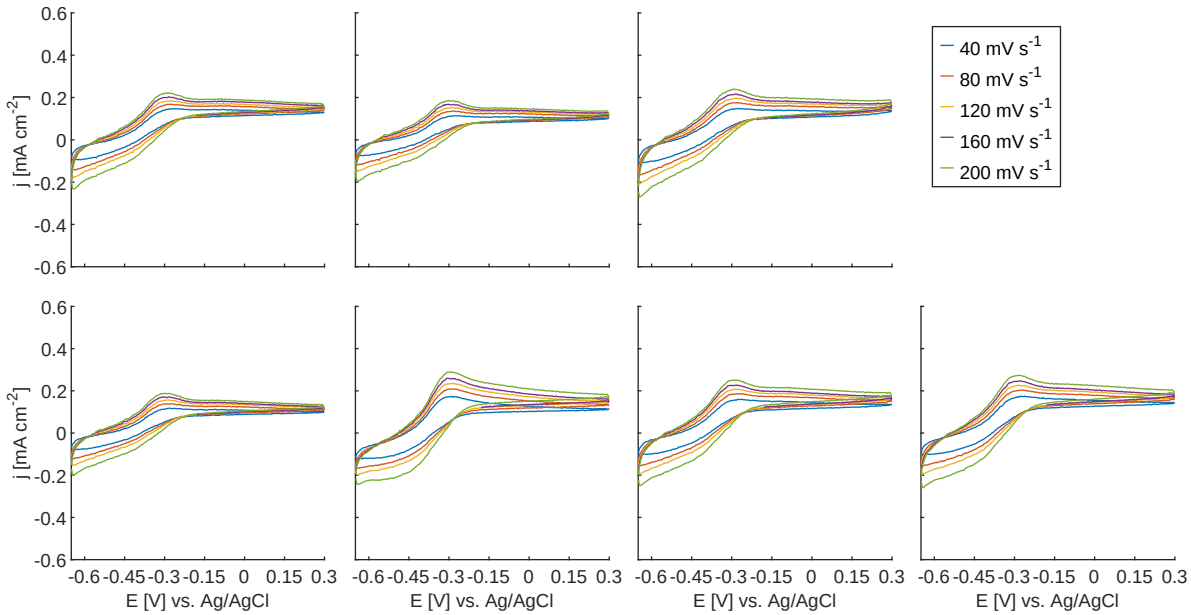

(f) −0.2 V vs. Ag/AgCl

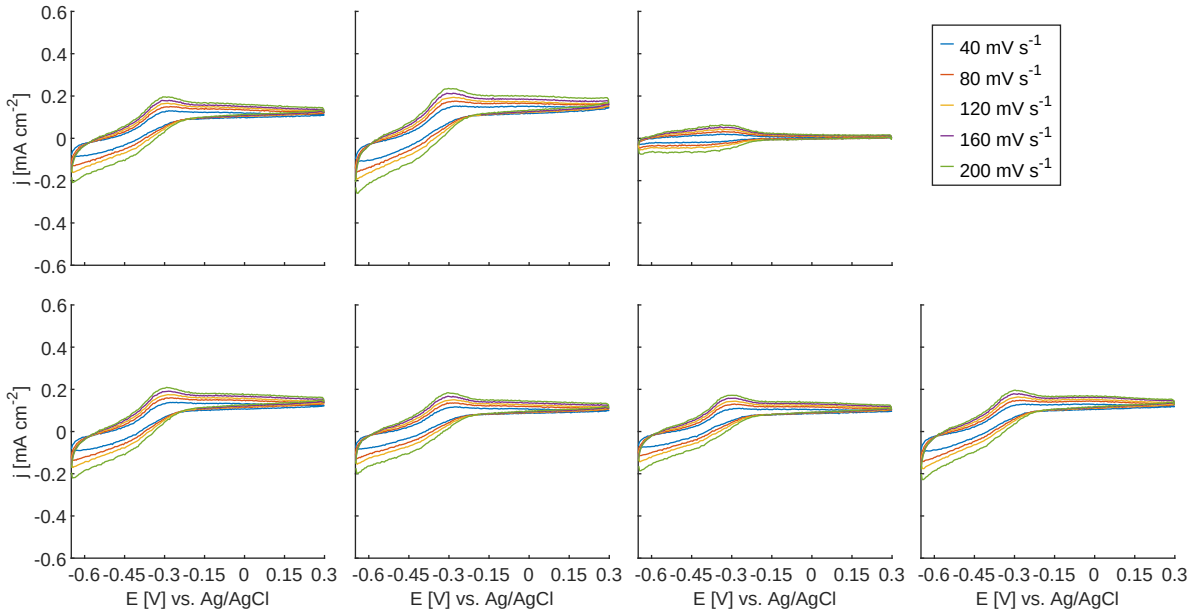

(g) −0.15 V vs. Ag/AgCl

Figure S11: (cont.) Nonturnover CVs for (f) −0.2 V vs. Ag/AgCl and (g) −0.1 V vs. Ag/AgCl after the second growth cycle for scan rates of 40 mV s^{-1} (blue), 80 mV s^{-1} (red), 120 mV s^{-1} (yellow), 160 mV s^{-1} (purple), and 200 mV s^{-1} (green). Electrodes are counted from left to right and top to bottom. Recorded after 324 h of polarization after inoculation.

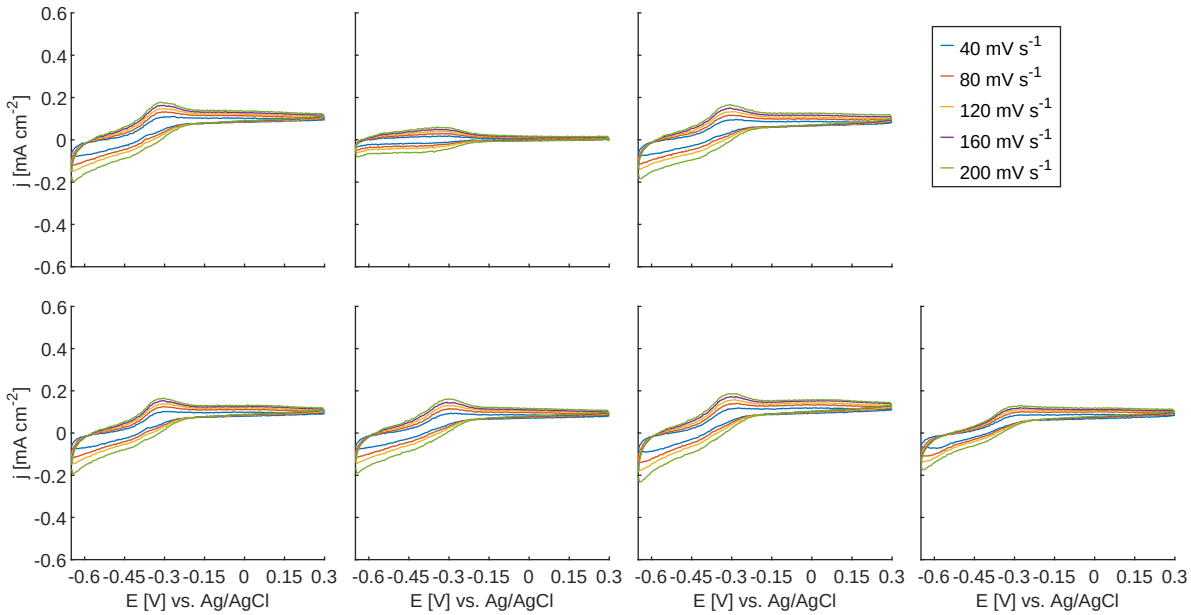

(h) −0.1 V vs. Ag/AgCl

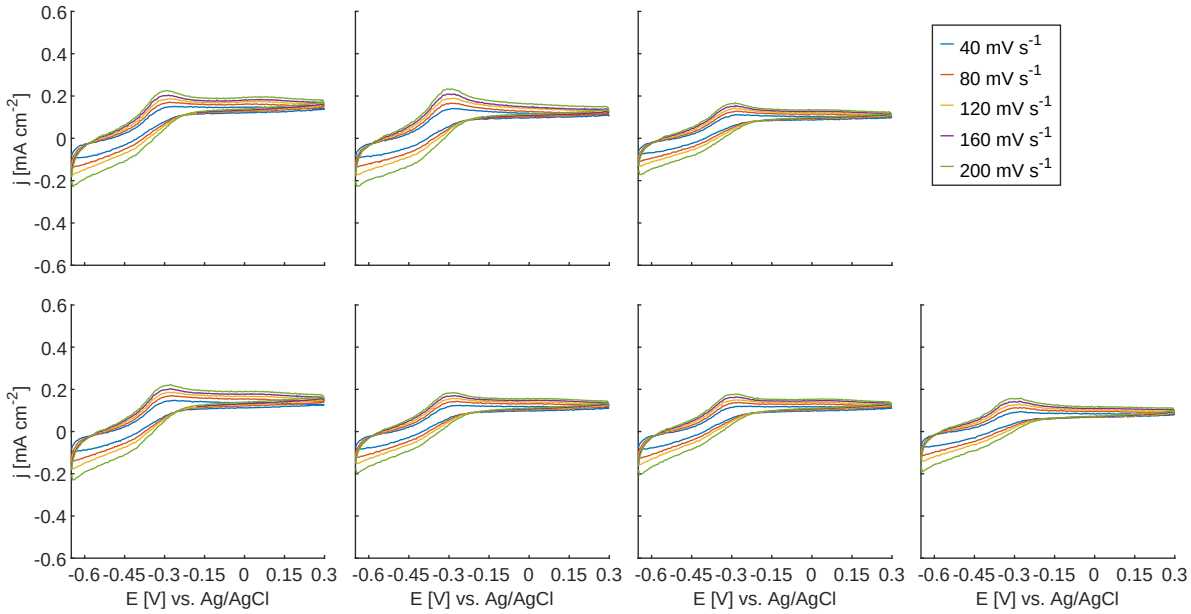

(i) 0 V vs. Ag/AgCl

Figure S11: (cont.) Nonturnover CVs for (h) −0.1 V vs. Ag/AgCl and (i) 0 V vs. Ag/AgCl after the second growth cycle for scan rates of 40 mV s^{-1} (blue), 80 mV s^{-1} (red), 120 mV s^{-1} (yellow), 160 mV s^{-1} (purple), and 200 mV s^{-1} (green). Electrodes are counted from left to right and top to bottom. Recorded after 324 h of polarization after inoculation.

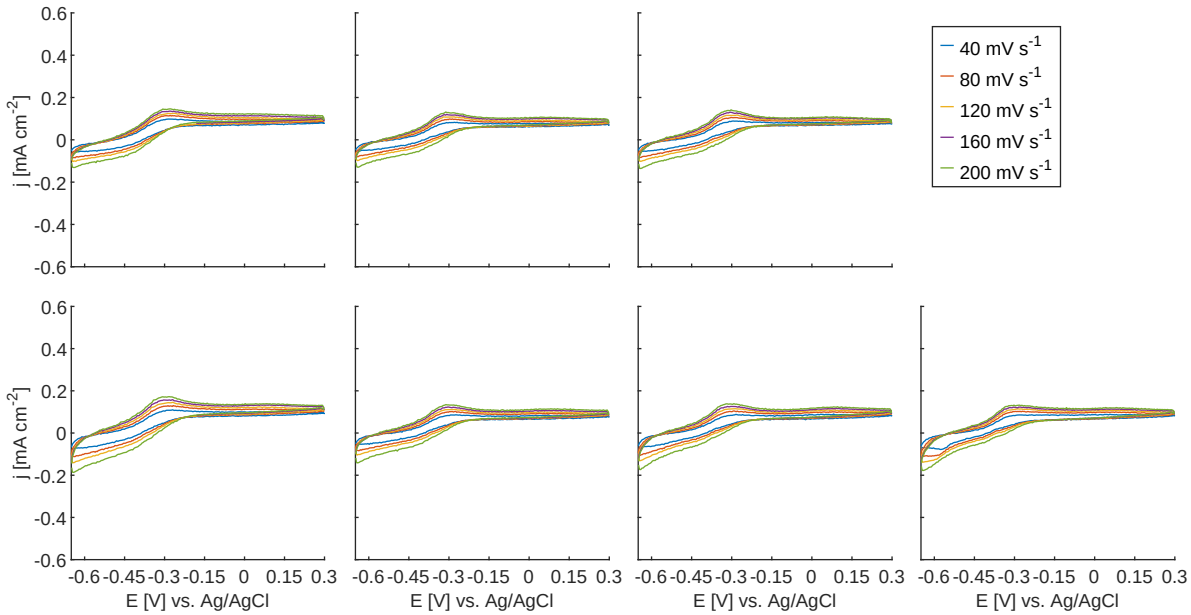

(j) +0.1 V vs. Ag/AgCl

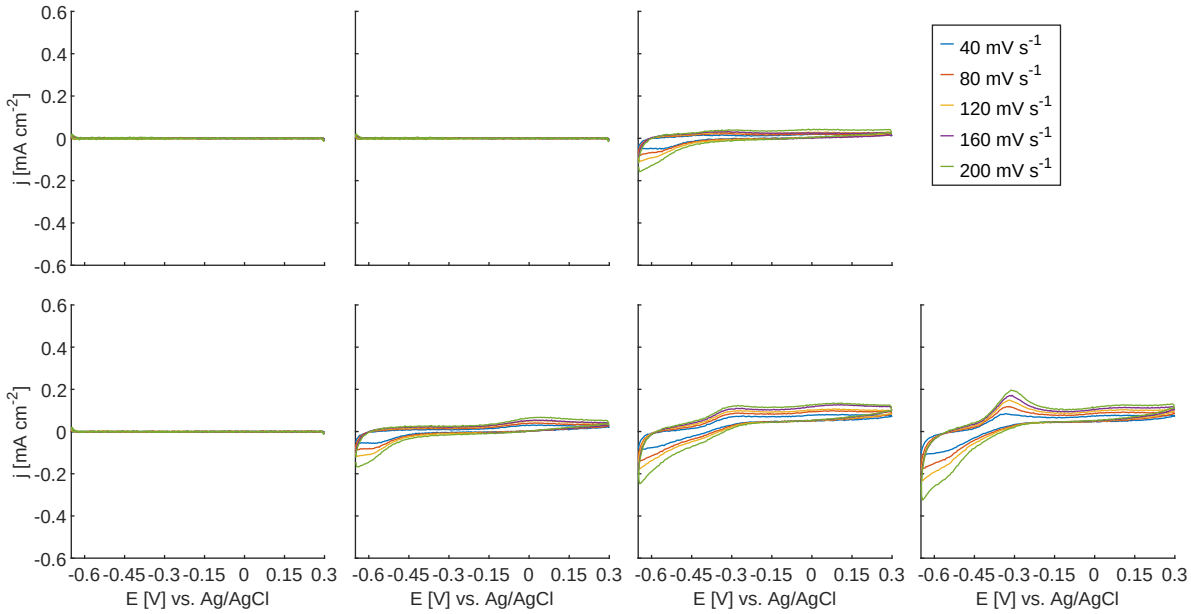

(k) +0.2 V vs. Ag/AgCl

Figure S11: (cont.) Nonturnover CVs for (j) +0.1 V vs. Ag/AgCl and (k) +0.2 V vs. Ag/AgCl after the second growth cycle for scan rates of 40 mV s^{-1} (blue), 80 mV s^{-1} (red), 120 mV s^{-1} (yellow), 160 mV s^{-1} (purple), and 200 mV s^{-1} (green). Electrodes are counted from left to right and top to bottom. Recorded after 324 h of polarization after inoculation.

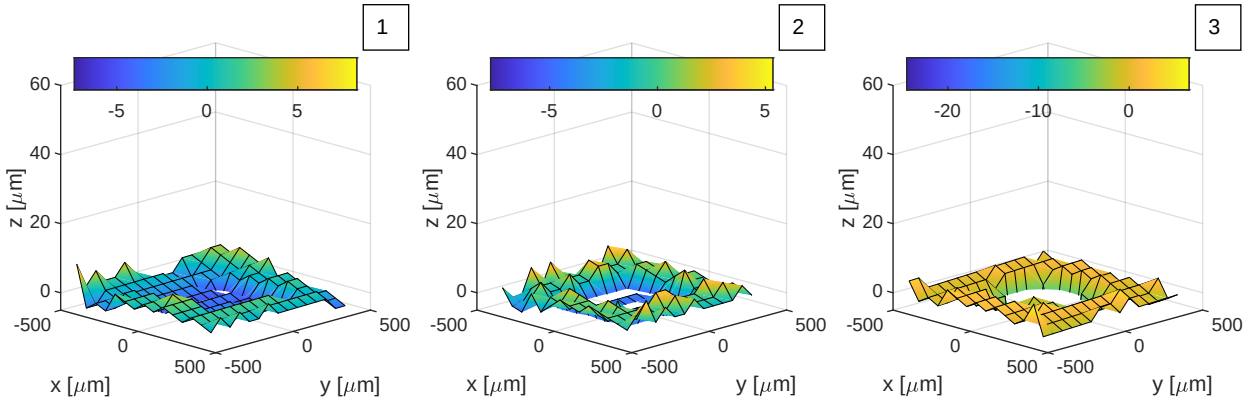

(a) −0.45 V vs. Ag/AgCl

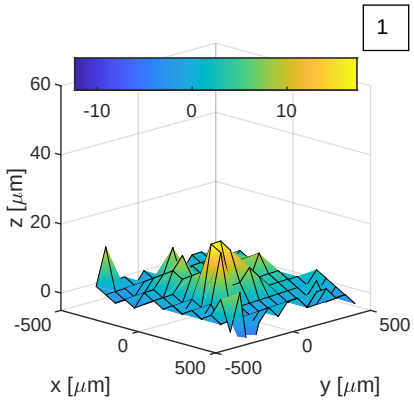

(b) −0.4 V vs. Ag/AgCl

Figure S12: Morphology of the EAB volume recorded by confocal microscopy for electrodes (a) −0.45 V vs. Ag/AgCl and (b) −0.4 V vs. Ag/AgCl.

9 EAB volume

Fig. S12 shows the morphology of selected EABs using confocal microscopy. Only 3 samples per potential range were analyzed. Of these, some failed (2 for −0.4 V, 1 for −0.25 V, 1 for −0.15 V, and 2 for +0.1 V), resulting in less than 3 reported EAB volumes for those electrode potentials.

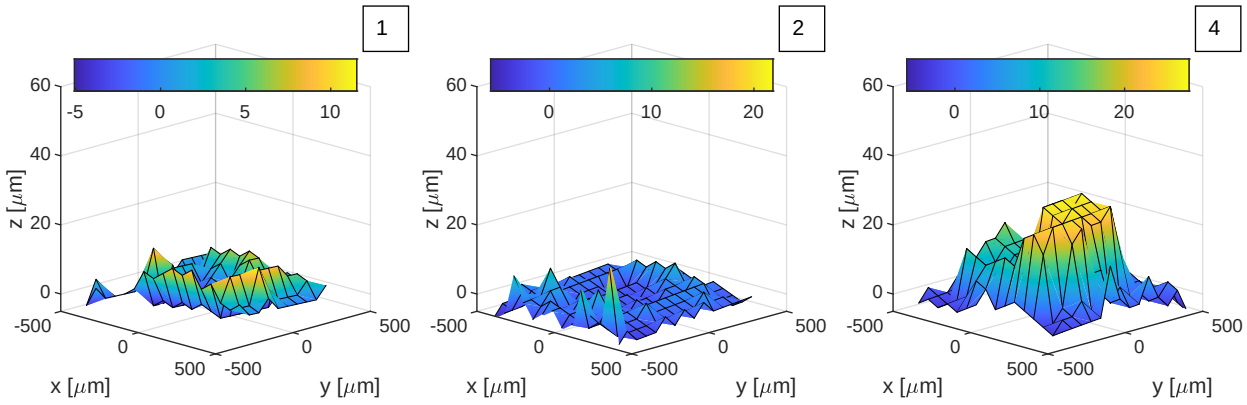

(c) −0.35 V vs. Ag/AgCl

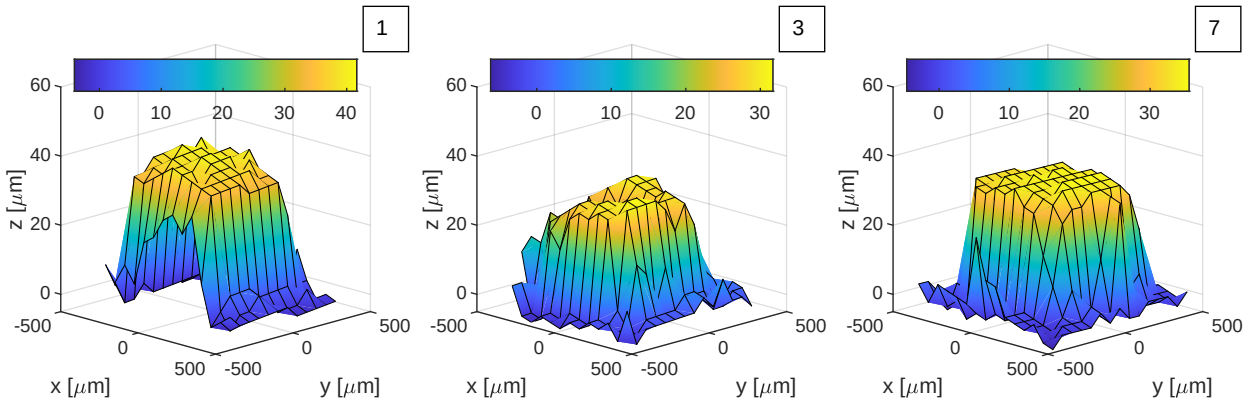

(d) −0.3 V vs. Ag/AgCl

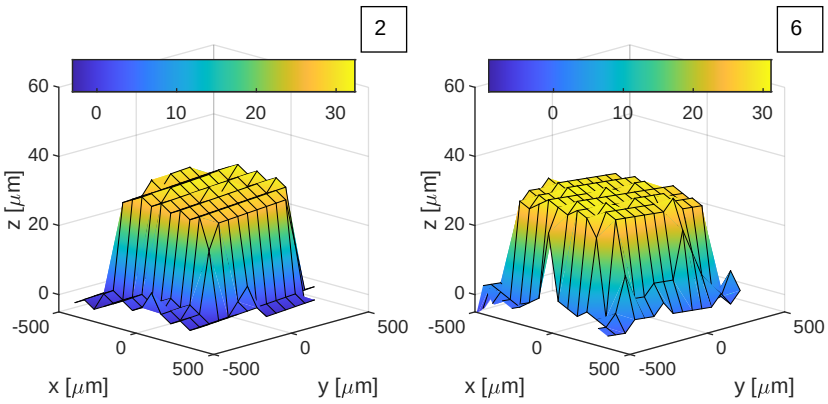

(e) −0.25 V vs. Ag/AgCl

Figure S12: (cont.) Morphology of the EAB volume recorded by confocal microscopy for electrodes (c) −0.35 V vs. Ag/AgCl, (d) −0.3 V vs. Ag/AgCl, and (e) −0.25 V vs. Ag/AgCl.

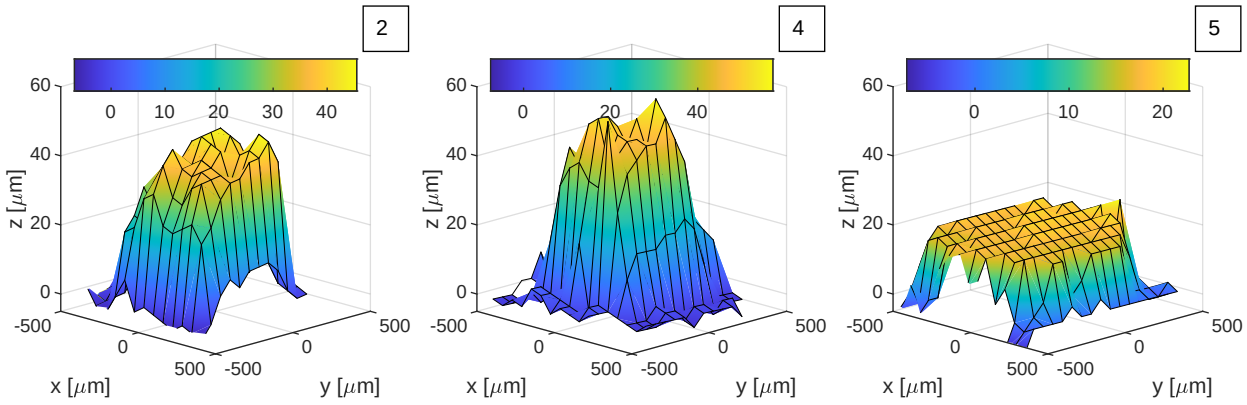

(f) −0.2 V vs. Ag/AgCl

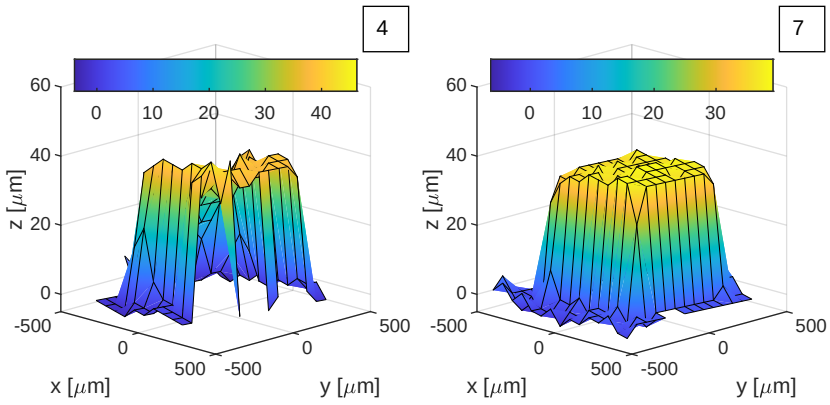

(g) −0.15 V vs. Ag/AgCl

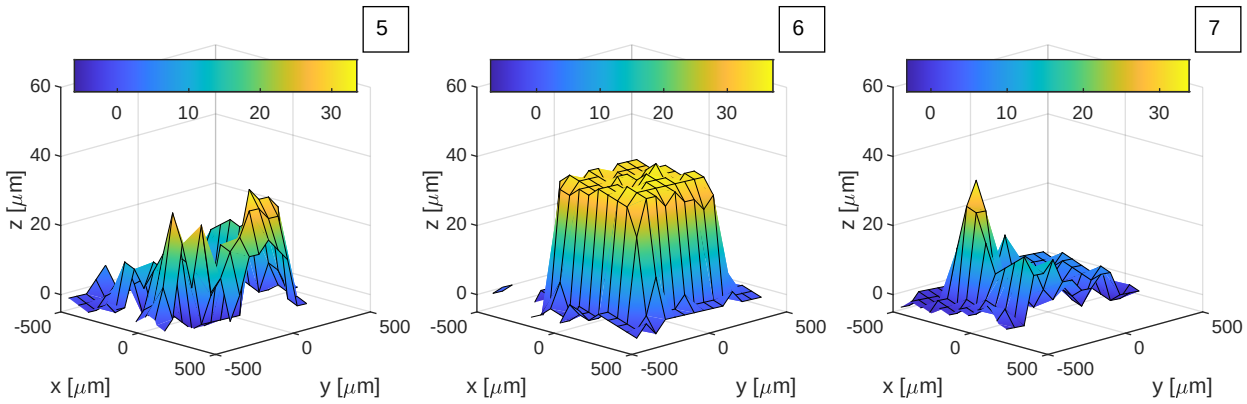

(h) −0.1 V vs. Ag/AgCl

Figure S12: (cont.) Morphology of the EAB volume recorded by confocal microscopy for electrodes (f) −0.2 V vs. Ag/AgCl, (g) −0.15 V vs. Ag/AgCl, and (h) −0.1 V vs. Ag/AgCl.

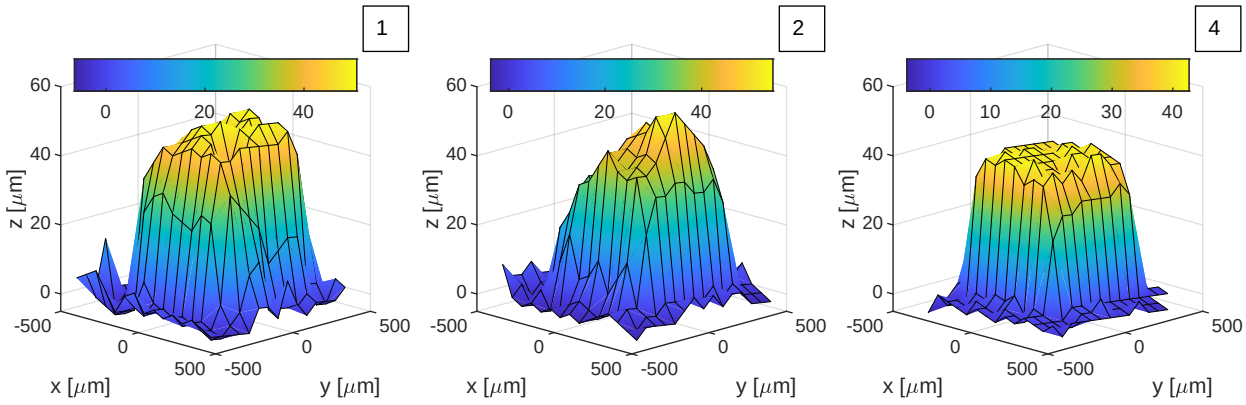

(i) 0 V vs. Ag/AgCl

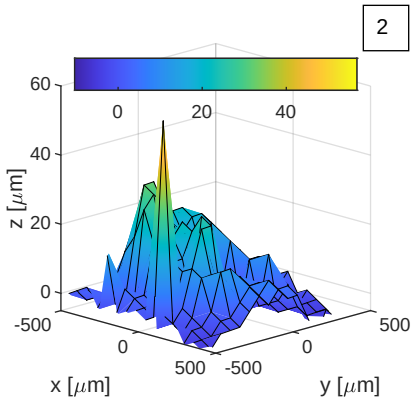

(j) +0.1 V vs. Ag/AgCl

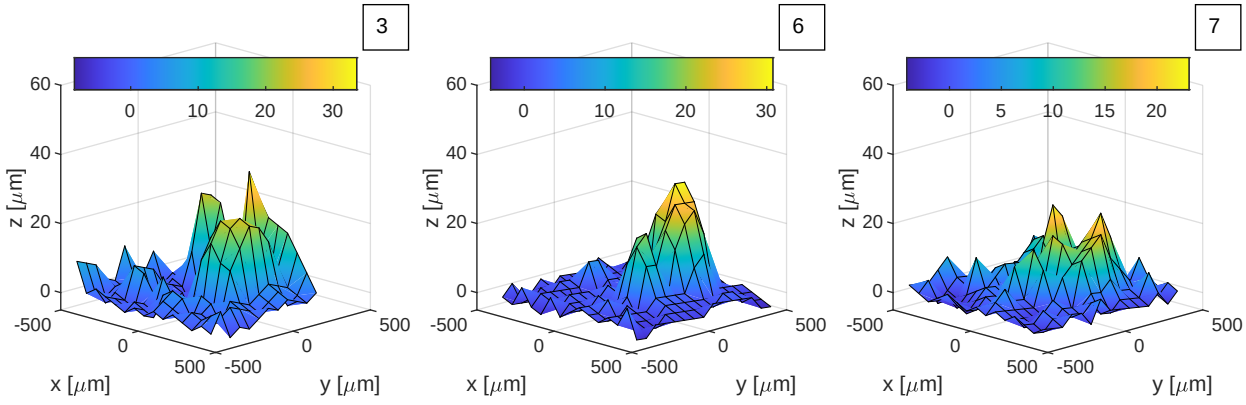

(k) +0.2 V vs. Ag/AgCl

Figure S12: (cont.) Morphology of the EAB volume recorded by confocal microscopy for electrodes (i) 0 V vs. Ag/AgCl, (j) +0.1 V vs. Ag/AgCl, and (k) +0.2 V vs. Ag/AgCl.

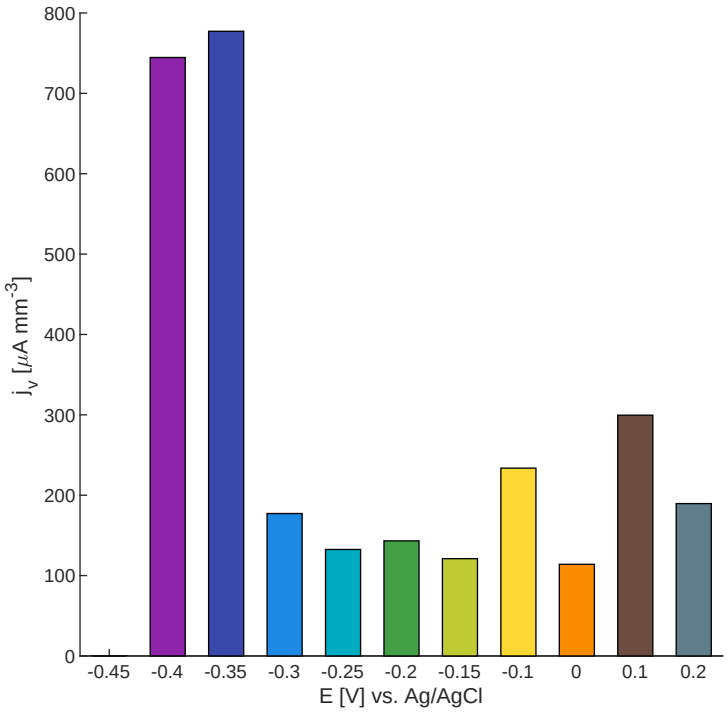

Figure S13: Current volume density of the EAB.

10 EAB volume current density

Based on the volume of the EABs and their recorded current density, the volume current density is calculated. The ordinary current density is somewhat biased for small electrodes due to the small expansion of the EAB out of the electrode boundary. Fig. S13 contains the maximum volume current density (during the second cycle).